Evaluating Convective Initiation in High-Resolution Numerical Weather Prediction Models Using *GOES-16* Infrared Brightness Temperatures

DAVID S. HENDERSON,[a] JASON A. OTKIN,[b] AND JOHN R. MECIKALSKI[c]

[a] *Space Science and Engineering Center, University of Wisconsin–Madison, Madison, Wisconsin*
[b] *Cooperative Institute for Meteorological Satellite Studies, University of Wisconsin–Madison, Madison, Wisconsin*
[c] *Atmospheric Sciences Department, University of Alabama in Huntsville, Huntsville, Alabama*

(Manuscript received 21 August 2020, in final form 28 January 2021)

ABSTRACT: The evolution of model-based cloud-top brightness temperatures (BT) associated with convective initiation (CI) is assessed for three bulk cloud microphysics schemes in the Weather Research and Forecasting Model. Using a composite-based analysis, cloud objects derived from high-resolution (500 m) model simulations are compared to 5-min *GOES-16* imagery for a case study day located near the Alabama–Mississippi border. Observed and simulated cloud characteristics for clouds reaching CI are examined by utilizing infrared BTs commonly used in satellite-based CI nowcasting methods. The results demonstrate the ability of object-based verification methods with satellite observations to evaluate the evolution of model cloud characteristics, and the BT comparison provides insight into a known issue of model simulations producing too many convective cells reaching CI. The timing of CI from the different microphysical schemes is dependent on the production of ice in the upper levels of the cloud, which typically occurs near the time of maximum cloud growth. In particular, large differences in precipitation formation drive differences in the amount of cloud water able to reach upper layers of the cloud, which impacts cloud-top glaciation. Larger cloud mixing ratios are found in clouds with sustained growth leading to more cloud water lofted to the upper levels of the cloud and the formation of ice. Clouds unable to sustain growth lack the necessary cloud water needed to form ice and grow into cumulonimbus. Clouds with slower growth rates display similar BT trends as clouds exhibiting growth, which suggests that forecasting CI using geostationary satellites might require additional information beyond those derived at cloud top.

SIGNIFICANCE STATEMENT: Several studies have used weather satellites to examine storm properties; however, they do not provide information about processes occurring within clouds. To address this limitation, we used numerical weather prediction model simulations and an object-based analysis method to learn more about in-cloud processes that influence the evolution of thunderstorms in the southeastern United States. The model and satellite comparison helped demonstrate that differences in the timing of rainfall formation can impact the amount of ice reaching the upper portion of the cloud. When ice forms, the cloud begins to grow rapidly and is more likely to become a long-lived thunderstorm. The results highlight the importance of using satellite data sensitive to clouds to evaluate the conditions under which cumulus clouds transition into severe storms.

KEYWORDS: Cloud microphysics; Convective storms; Satellite observations; Model comparison; Model evaluation/performance; Numerical analysis/modeling

1. Introduction

In the southeastern United States, the quick onset of isolated thunderstorms with heavy rainfall is commonly observed (Rickenbach et al. 2015). Accurate prediction of the onset time, location, and evolution of convection continues to be a difficult problem for observational and numerical weather prediction (NWP) models (e.g., Kain et al. 2013; Mecikalski et al. 2015; Lawson et al. 2018; Cintineo et al. 2020). When tracking growing cumulus clouds using radar and satellite observations, convective initiation (CI) is commonly referred to as the time during which growing convection contains a radar reflectivity ≥ 35 dBZ because that threshold is highly correlated to convection that eventually develops into a mature cumulonimbus cloud (Roberts and Rutledge 2003; Mecikalski and Bedka 2006). CI in the southeastern United States, particularly during the spring and summer months, can be complicated to forecast as cumulus clouds are often more isolated, and driven primarily by strong surface heating (Gambill and Mecikalski 2011; Miller and Mote 2017; Kirshbaum et al. 2016; Rickenbach et al. 2020). Such isolated weakly forced thunderstorms can also be initiated by subtle variations in surface heating and evaporation caused by land-use variations and topography (Gambill and Mecikalski 2011) and by small lakes (Asefi-Najafabady et al. 2012). Once convection begins, subsequent isolated convective cells typically are initiated by outflow boundaries from the surrounding convection (Goggins et al. 2010).

To help mitigate difficulties in forecasting the onset of CI, several methodologies have been developed to make use of geostationary satellite platforms to improve CI nowcasting lead times (Roberts and Rutledge 2003; Mecikalski and Bedka 2006; Mecikalski et al. 2010; Sieglaff et al. 2011; Walker et al. 2012). Along with these tracking methods, implementing combinations of the satellite brightness temperature (BTs) and

Corresponding author: David Henderson, dshenderson@wisc.edu

DOI: 10.1175/MWR-D-20-0272.1

their tendencies, or so-called satellite-based interest fields, have been developed to aid the prediction of CI and the onset of heavy precipitation and lightning (e.g., Mecikalski and Bedka 2006; Harris et al. 2010). However, even when using auxiliary information about the environmental conditions, false positive detection remains an issue (Mecikalski et al. 2015). The higher spatial and temporal resolution available from the current generation of geostationary satellites have demonstrated improvements in describing the evolution of cloud characteristics associated with intense convection (e.g., Senf and Deneke 2017; Apke et al. 2018). Senf and Deneke (2017) and Patou et al. (2018) demonstrated that tracking cloud-top cooling and cloud-top hydrometeor phase are important factors when identifying clouds that will likely transition to heavy precipitation. Patou et al. (2018) and Mecikalski et al. (2015) demonstrated that connecting tracked-cloud features in satellite observations with output from NWP model forecasts has the potential to improve our understanding of the trigger mechanisms leading to CI.

The main motivation for this study was to increase understanding of the processes leading to CI in weakly forced environments through application of object-based CI composites commonly used in CI satellite nowcasting studies. Application of the satellite-based techniques provides a novel method to evaluate high-resolution models using established satellite-based metrics. NWP models allow in-cloud processes to be resolved, but as NWP resolution has increased the representation of CI location and timing has thus far shown limited improvement (Kain et al. 2008; Schwartz et al. 2009; Langhans et al. 2013; Burghardt et al. 2014). Evaluating model performance using standard point-by-point methods is difficult at higher resolutions because small positioning errors in the forecast may be penalized for not forecasting the event at the observation point even though qualitatively it may be a better forecast. Improvements in CI forecasting have been demonstrated when assimilating surface observations (Liu and Xue 2008; Sobash and Stensrud 2015); however, forecasting on the meso-α storm scale (2.5–25 km) requires a high-density network of surface (Madaus and Hakim 2016, 2017) or satellite observations (e.g., Yussouf et al. 2015; Zhang et al. 2019; Jones et al. 2020). Further, forecasts from model simulations can drastically change in relation to the assumptions in the model setup (e.g., Otkin and Greenwald 2008; Cintineo et al. 2014; Griffin et al. 2017), and the accuracy of storm location and timing remains an issue (Weisman et al. 2008; Mittermaier and Bullock 2013; Shrestha et al. 2013; Bytheway and Kummerow 2015, 2018). Because satellite and radar observations alone are unable to fully resolve CI, additional insight concerning processes occurring within the cloud are needed to improve forecast accuracy. This can be accomplished using high-resolution NWP simulations that provide information about in-cloud microphysical processes. To apply knowledge gained from simulated cloud properties to observations, however, we must ensure that the forecasted cloud properties are representative of the convection reaching CI. Convection produced in weakly forced environments, that commonly occur in the Southeastern United States, therefore provides the opportunity to evaluate CI processes driven largely by cloud microphysics in conditions devoid of large synoptic forcing.

Linking output from NWP models to geostationary satellite observations has been accomplished by previous studies through the use of radiative transfer models to simulate satellite BTs (e.g., Tselioudis and Jakob 2002; Lopez et al. 2003; Grasso and Greenwald, 2004; Otkin and Greenwald 2008; Otkin et al. 2009; Cintineo et al. 2014; Lee et al. 2017; Thompson et al. 2016; Griffin et al. 2017; Bytheway et al. 2017; Griffin et al. 2020; Kim et al. 2020). These studies track and compare mean characteristics of clouds as a whole, yet lack an ability to evaluate cloud morphology. Work is therefore needed in order to track specific processes driving individual convective cells evolving from shallow cumulus to clouds that deepen and produce heavy precipitation within an environment with little to no mesoscale or synoptic-scale variability. Comparing the observed and simulated BTs can be challenging due to timing and location errors in the forecast cloud objects, which makes point-to-point comparisons with traditional verification methods difficult (Griffin et al. 2017). Object-based analysis can improve these comparisons by accounting for spatial displacement errors (e.g., Burghardt et al. 2014; Griffin et al. 2017; Bytheway and Kummerow 2018). This study will build upon prior work that has primarily focused on larger cloud systems by examining the evolution of individual convective cells in a weakly forced environment.

The high-temporal-resolution data from the *GOES-16* Advanced Baseline Imager (ABI; Schmit et al. 2017) provides an ideal dataset to track the life cycle of convection because the temporal resolution of 1–5 min is more in line with the time scales of cumulus cloud growth (Gravelle et al. 2016). For this study, individual convective cells produced by high-resolution Weather Research and Forecasting (WRF) Model simulations will be tracked and evaluated using geostationary-derived CI interest fields to understand how bulk microphysical parameterization schemes represent the formation and development of hydrometeor species, cloud growth, and precipitation processes. We present a strategy to evaluate the evolution of simulated convection using recent observation-based tracking techniques in parallel with recent methods used to describe CI in observational-based studies (e.g., Harris et al. 2010; Mecikalski et al. 2011, 2016a; Senf and Deneke 2017). Mecikalski et al. (2011) demonstrated that satellite BT CI interest fields describing cloud growth are most beneficial when nowcasting CI using geostationary satellites, specifically using Meteosat Second Generation data, which mimics those from *GOES-16*. These CI interest fields will be computed using *GOES-16* ABI observed and simulated model BT imagery, and then compared in lag-based composites of cloud objects as a function of the timing of CI. This composite-based method focuses the evaluation on the model ability to simulate the evolution of convection independent of the cloud location and time. The evaluation will also be applied to gain greater understanding of the cloud processes occurring within the clouds that lead to various cloud-top signatures depicted in satellite infrared (IR) imagery. Going forward, the paper is structured as follows: The case analysis, model setup, and observational

data are described in section 2, and the cloud tracking technique and methods are described in section 3; analysis of the WRF simulations and discussion of the results are shown in section 4, with a summary of the overall findings provided in section 5.

2. Data and model setup

a. Geostationary data

This analysis will employ observations from the *GOES-16* ABI sensor (Schmit et al. 2017). Individual and combinations of ABI bands will be assessed that together provide a detailed depiction of the cloud properties in different parts of the troposphere (Fig. 2 in Schmit et al. 2017). The ABI IR BTs from spectral window regions are highly sensitive to cloud particles in the uppermost portion of a cloud and therefore provide valuable information about the horizontal and vertical extent of the clouds. The emphasis on IR channels in this work ensures continuous day–night cloud observations. The 2-km-resolution IR channels on the ABI sensor also allow for a more accurate discrimination of liquid and ice clouds that are crucial to evaluate the various mixed-phase and ice processes in a bulk microphysics parameterization scheme, as found by Mecikalski et al. (2010, 2015) and Senf and Deneke (2017). BT-derived forecast factors used in this study include the evolution in cloud-top height (10.35 μm channel), cloud growth tendencies (10.35 μm BT tendency every 5 min), and channel differences providing cloud-top glaciation estimates (8.4–10.35 μm BT difference). These *GOES-16* ABI channels are available over CONUS every 5 min, which permits more frequent comparisons with the WRF output compared to previous satellite sensors. This in turn supports a more detailed comparison of clouds evolving in CI events, particularly the early stages of convection that may have been missed previously due to limited temporal resolution (Mecikalski et al. 2008).

b. Ground radar data

Ground-based NEXRAD S-band data for three radar sites located in Alabama and Mississippi (KBMX-Birmingham, KGWX-Columbus, and KDGX-Jackson) are used in this analysis. The spatial coverage of these radars is shown by the blue circles in Fig. 1. The NEXRAD data comes from Doppler weather radars that operate at S-band (10 cm) and level 2 data are collected for the vertically resolved radar reflectivity. Volume scan data for the three radar sites are converted to a 1 km horizontal and vertical cartesian grid using the open-source Python Atmospheric Radiation Measurement Radar Toolkit (Helmus and Collis 2016). Composite reflectivity data are created from the gridded data using the maximum reflectivity at each grid point and then the four closest reflectivity data points are matched to the closest 2 km *GOES-16* IR observation. Radar scanning intervals are not constant due to changes in radar volume coverage for a particular scan; therefore, we collocate the radar data to the nearest 5 min *GOES-16* observations. Application of the radar reflectivities to CI identification is described in section 3.

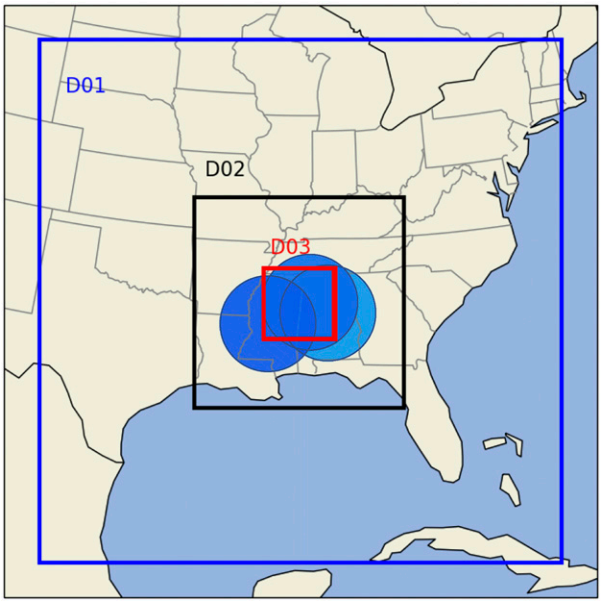

FIG. 1. Illustration of the three WRF Model domains. Convective initiation is assessed within the inner domain (D03) using *GOES-16* observations and data from three WSR-88D sites (blue circles).

c. WRF Model setup and simulated brightness temperatures

The WRF-ARW Model (version 3.9.1.1) is used to simulate a case study from 20 May 2018 that was characterized by weakly forced deep convection across Alabama and Mississippi during the afternoon and evening. A ridge over the domain brought a typical summer weather pattern to the Mississippi and Alabama region that is devoid of major synoptic forcing mechanisms and wind shear, yet with moderate afternoon instability. High pressure located off the eastern coast of the United States provided the region with abundant moisture from the Gulf of Mexico. The 0000 UTC 21 May BMX sounding (not shown) indicates a freezing level near 4000 m and a warm layer near 5800 m. CAPE was above 1500 J kg^{-1} and surface temperatures exceeded 90°F, but moderate convective inhibition is observed with CIN near −40 J kg^{-1}. Convection able to surpass this warm lid would be able to grow toward deep convection across the entire region during the afternoon and evening hours. Multiple slow-moving isolated convective cells with damaging wind gusts and hail occurred across the region according to storm reports from the Storm Prediction Center. Slow-moving convective features such as these are common in late spring and summer across this region and allow for easier tracking with satellite and radar observations. To capture the finescale convective features associated with this event, three two-way feedback permitted WRF Model domains are used with nests possessing 12.5 km, 2.5 km, and 500 m resolution, respectively, centered over Alabama and Mississippi (Fig. 1). The initial and lateral boundary conditions are provided every 6 h by the National Centers for Environmental Prediction final (NCEP FNL) analyses on a 0.25° latitude–longitude grid. The WRF Model

simulations contain 53 sigma levels, with the model top set to 25 hPa.

Three commonly used bulk microphysics schemes are examined in this study: the Thompson et al. (2008), Morrison (Morrison et al. 2005, 2009), and WRF double-moment 6-class (WDM6; Lim and Hong 2010) schemes. All of these microphysics schemes predict mass mixing ratios of cloud water, rainwater, cloud ice, snow, and graupel. The Thompson and WDM6 are mixed- moment schemes, where WDM6 predicts two-moments (mixing ratio and number concentration) in warm rain processes and the Thompson scheme predicts two-moments of cloud water and ice. The two-moment Morrison scheme predicts mixing ratios for all cloud hydrometeor categories and number concentrations are also predicted for cloud ice, snow, rain, and graupel. Each microphysics scheme allows output of a radar reflectivity factor based on the Rayleigh approximation, which is very similar to the S-band wavelength observations of our ground-based radar data.

All WRF simulations use an identical model configuration, apart from the microphysics scheme. Simulations are initialized at 1200 UTC, which allows sufficient model spinup as the first CI case occurs near 1700 UTC. Physics options included are the Rapid Radiative Transfer Model for Global Climate Models (RRTMG; Iacono et al. 2008), the nonlocal-mixing Yonsei University (YSU; Hong et al. 2006; Lim and Hong 2010) planetary boundary layer scheme, and the Noah-MP land surface model (Niu et al. 2011). No cumulus parameterization is used on the higher-resolution 2.5 km and 500 m domains, whereas the Tiedtke (Tiedtke 1989; Zhang et al. 2011) scheme is used on the outermost 12.5 km domain.

The evolution of CI events will be assessed on the high-resolution 500 m innermost domain. Data were output every 5 min to be consistent with the temporal resolution of CONUS *GOES-16* ABI data. Following Griffin et al. (2017), the Community Radiative Transfer Model version 2.1 (CRTM; Ding et al. 2011) was used to convert the WRF Model output into simulated *GOES-16* ABI IR BT data. The CRTM provides all-sky top-of-the-atmosphere BTs that incorporate the *GOES-16* viewing geometry for channels 7–16 of the ABI (3.9–13.3 μm). Top-of-the-atmosphere BTs in clear-sky scenes are generated using surface emissivity provided by the University of Wisconsin High Spectral Resolution Emissivity Algorithm (Borbas et al. 2007), and WRF Model predicted surface skin temperature, 10 m wind speed, and vertical profiles of temperature, pressure, and water vapor mixing ratio. Cloudy scenes use the above information, as well as derived cloud properties (i.e., effective particle radius, cloud water content) consistent with the assumptions made by each cloud microphysics parameterization scheme used (e.g., Otkin et al. 2007; Thompson et al. 2016; Griffin et al. 2017). Cloud properties were derived individually for each cloud species and input into the CRTM to compute the cloud optical properties (i.e., single scatter albedo, asymmetry parameter, and full scattering phase function) for each model grid point and vertical layer. Finally, the combined set of hydrometeor optical properties were used to compute the top-of-the-atmosphere BT data for each IR band measured by the ABI.

3. Cloud object identification and CI compositing

a. Cloud object and CI identification

Cloud tracking and detection methods are applied identically for the observed and simulated BT datasets. Cloud tracking is based on 10.35 μm BTs because radar observations may not be available during the entire cloud life cycle (Mecikalski and Bedka 2006). Cloud objects are identified based on the Tracking Of Organized Convection Algorithm through 3D segmentation (TOOCAN; Fiolleau and Roca 2013) algorithm and tracked through time when overlapping areas occur in successive images of cloud objects (e.g., Vila et al. 2008). This tracking scheme takes advantage of the fact that IR BTs are sensitive to cloud particles (their size, phase, and amount) in the upper portion of the cloud giving extensive information on the horizontal and vertical extents of cloud tops, which helps separate cloud clusters through time. Using this iterative method of tracking clouds using the IR channels has been shown to be effective tracking intense convection (e.g., Wall et al. 2018; Cancelada et al. 2020).

To maintain consistency with the ABI observations, model gridded BTs are averaged to 2 km grid spacing when identifying objects. Inspection of the BT imagery showed that the coldest cloud tops during the observation period have BT $<$ 210 K. Thus, cloud boundaries are first searched for using BT $<$ 210 K and then iteratively increasing by 2.5 K to detect cloud boundaries (Fig. 2), where the warmest cloud boundaries within this case study are defined as where the 10.35 μm BTs are $<$ 285 K. This warm cloud boundary threshold helps capture cloud growth before CI is detected, but also ensures that possible surface BT contamination is excluded. Fiolleau and Roca (2013) describe the cloud detection as iteratively growing cloud ''seeds'' from colder to warmer BTs. In this work, clouds are identified using the TOOCAN methodology by detecting initial boundaries using a low BT threshold of 210 K. For each identified object, pixels are added to the cold cloud-top object using a 2.5 K warmer BT threshold to identify the edge of the new boundary. The warmer BT threshold is also applied to detect new cloud object ''seeds.'' This iterative process of extending the cloud boundary by 2.5 K is repeated until each of the grid boxes within a cloud object are colder than 285 K or if cloud overlap is detected with a neighboring object. Once cloud objects are identified for each 5-min time step from the observations and simulations, the SciPy data package (Virtanen et al. 2020) is used to detect and track the cloud object overlap between time steps.

To be consistent with previous observational studies (e.g., Roberts and Rutledge 2003; Mecikalski et al. 2006; Weckwerth and Parsons 2006), a cloud object from the *GOES-16* ABI and WRF simulations will be defined as CI when radar reflectivity $>$ 35 dBZ occurs in a cloud object. This threshold is common in thunderstorm nowcasting studies where CI is exclusively defined using a radar precipitation echo intensity criteria of $\geq$30–40 dBZ (Browning and Atlas 1965; Marshall and Radhakant 1978; Schreiber 1986; Wilson and Schriber 1986; Wilson et al. 1992; Wilson and Mueller 1993; Mueller et al. 2003; Walker et al. 2012; Lee et al. 2017; Han et al. 2019). The 35 dBZ threshold signifies convective precipitation near the surface of

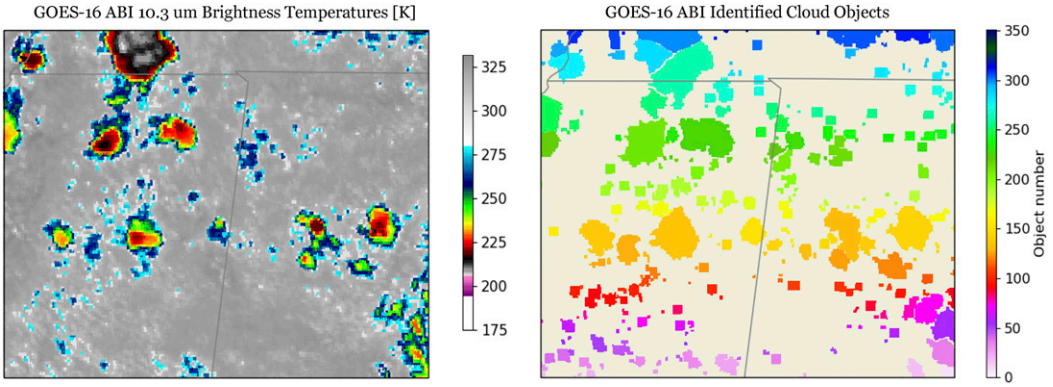

FIG. 2. (left) An example of 1900 UTC *GOES-16 ABI* 10.35 μm brightness temperatures (K) within the inner domain region. (right) Derived cloud objects from this time step.

$\sim$8 mm h^{-1}. Clouds reaching this threshold typically produce significant precipitation, but it does not guarantee that the CI events will lead to long-lived convective storms (Mecikalski et al. 2015). To mitigate vertical resolution differences between NEXRAD and the model vertical grid we define CI when the maximum reflectivity in the cloud column exceeds 35 dBZ (e.g., Matthee et al. 2014; Senf and Deneke 2017).

b. *Composite analysis methodology*

Several physical cloud characteristics from observed and simulated cloud objects reaching CI are tracked and compared using lag-composite analysis. When the radar reflectivity within a cloud object surpasses the 35 dBZ threshold, that time step is labeled time lag zero and the data before, during, and after this CI time step are composited to describe the evolution of the cloud objects. Objects reaching CI are examined and compared when the cloud persists longer than 35 min to track the cloud evolution 15 min before and 15 min after the 5-min period in which CI is detected. Composited data includes the CI forecast interest fields described in section 2a, cloud area (defined using the number of grid boxes in the cloud object), and model-based properties from profiles of mixing ratios for each of the hydrometer types. After cloud objects are identified for each time lag, the cloud characteristics and CI forecast interest fields are derived. For *GOES-16* ABI data, the BT interest fields described in section 2a are derived using the grid boxes containing the two coldest 10.35 μm BTs within the cloud object (e.g., Mecikalski et al. 2010). For the WRF simulations, the coldest two grid boxes that were averaged to 2 km within each cloud object are used to derive the CI forecast interest fields, which is 32 grid boxes at 500 m grid spacing. If cloud objects are smaller than the grid boxes required for averaging the observed or modeled cloud objects, then all cloudy grid boxes are used with the cloud object boundaries.

4. Results

a. *Comparison of domain-based characteristics*

Cloud objects are compared over a 3-h period beginning at 1700 UTC, which is near the time the first CI object was observed in *GOES-16*. Table 1 provides a summary of the total cloud objects and CI cases tracked, and the time of first CI occurrence. This 3-h period is chosen to provide a sufficient number of objects, but also to limit new CI events that originate under larger cloud anvil regions where passive satellite observations cannot accurately discriminate multilayer cloud structures (Mace and Wrenn 2013). Model and observed cloud objects are first compared using domainwide statistics to understand the characteristics of the cloud objects without considering the stage of the cloud life cycle. The first observed *GOES-16* CI event occurs at 1655 UTC, with the first CI occurring at 1645, 1640, and 1700 UTC for the Thompson, Morrison, and WDM6 schemes, respectively. Overall, the Thompson and Morrison schemes produce more CI objects than was observed in *GOES-16* data, whereas the WDM6 simulation more accurately represents the number of observed CI objects.

CI cases over the 3-h period and their occurrence, fractional coverage, and cloud object areas are illustrated in Fig. 3. In Figs. 3a and 3b the number of CI cases that are active at each time step are represented by the solid lines and in Fig. 3c the range of CI cloud object areas are represented by the box-and-whisker diagrams. The data are plotted at 15-min intervals starting at 1700 UTC. The number of CI cases in the Morrison scheme quickly increases 30 min after the start of the observation period; however, the WDM6 scheme has a delay in occurrence compared to the other simulations and observations. Overall, the observations and simulations show an

TABLE 1. Number of total cloud objects colder than 285 K, number of CI objects tracked, and time of first-tracked CI cloud in the *GOES-16* observations and the Thompson, Morrison, and WDM6 simulations.

	Total cloud objects BT $<$ 285 K	No. of CI tracked	Time of first CI (UTC)
GOES-16	546	52	1655
Thompson	1853	121	1645
Morrison	2160	136	1650
WDM6	1946	67	1700

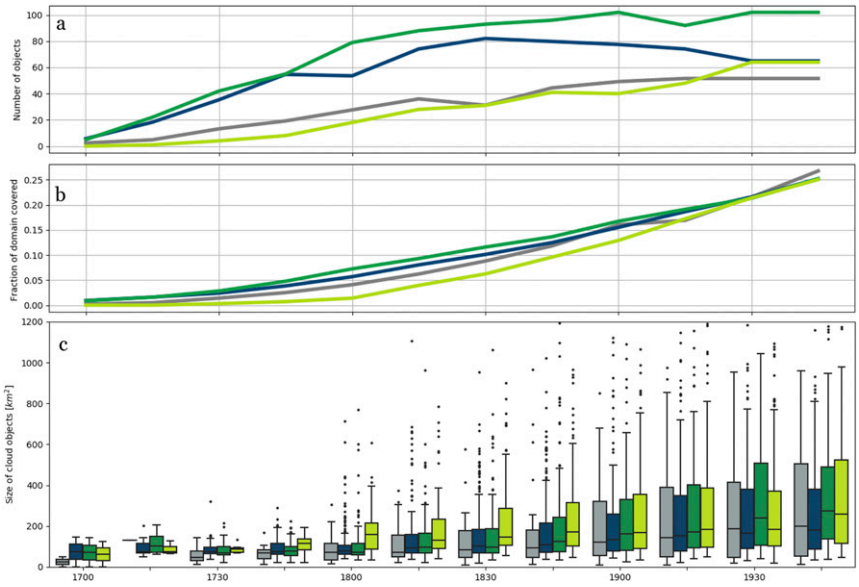

FIG. 3. The (a) occurrence of active CI cloud objects containing a reflectivity higher than 35 dBZ at each time step, (b) fractional coverage of active CI cloud objects, and (c) sizes of CI cloud objects for *GOES-16* (gray) observations and Thompson (blue), Morrison (green), and WDM6 (light green) simulations. Occurrence is shown by the solid lines and the spread of cloud object sizes is shown using the box-and-whisker diagrams.

increase in cloud object area over time. When compared to the observations (gray bars) the ranges in active CI cloud sizes from the simulations display a general agreement in median cloud object area throughout the 3-h period where the ranges in object size are close to the *GOES-16* observations.

The fractional coverage of active cloud objects (Fig. 3b) is similar to the pattern of CI occurrence (Fig. 3a) for each configuration, with the Thompson and Morrison schemes producing more objects covering a larger fractional than the WDM6 scheme. From 1700 UTC to around 1900 UTC, the Thompson and Morrison cloud object size interquartile range (IQR) shown in Fig. 3c is similar to observations, but the simulations contain more active cloud objects leading to a higher fraction of domain coverage (Fig. 3b). As clouds get larger toward the end of the observed period the fractional coverage for all simulations merge toward the observations, but the Morrison simulation contains more objects (Fig. 3a) and the Thompson cloud object size IQR is smaller than indicated by the *GOES-16* observations at 1945 UTC (Fig. 3c). This suggests that the Thompson and Morrison simulations produce too many small cloud objects compared to observations. The WDM6 simulation has a delay in occurrence, which leads to a lower fractional coverage throughout most of the observed period (Fig. 3b). The WDM6 simulation contains a higher cloud object size IQR starting around 1800 UTC, where CI cloud growth becomes more rapid than the other two microphysics schemes and cloud object occurrence and fractional coverage begins to move closer to the *GOES-16* observations. Further insight into microphysical reasonings leading to this delay in CI development for the WDM6 scheme will be provided in section 4b.

To investigate how the cloud height evolves within the cloud objects, Fig. 4 displays normalized frequency distributions of 10.35 μm BT for four different times in the WRF forecasts for all objects in a time step. Figure 5 shows the 10.35 μm BTs at 1900 UTC for the observations and model simulations. Inspection of Fig. 4 shows that there is a shift from shallow convection at 1700 UTC (mostly warmer BTs) toward a mix of shallow, congestus, and deep convection from 1800 to 1900 UTC (higher percentage of colder BTs), and predominantly deep convection with anvil regions at 2000 UTC. In the Morrison simulation, a higher fraction of convection occurs at 1800 UTC for BT near 260 K, whereas the WDM6 and Thompson schemes simulate a higher fraction of cloud tops colder than what was observed by the *GOES-16* ABI. Quantitively, this bias is found in the coldest cloud objects, which are compared using the coldest 10th percentile of 10.35 μm BT (Table 2) derived using a cumulative distribution function sorted by cloud-top temperature. Cold biases are largest in the Morrison scheme at 1700 UTC and continue through 1800 UTC. Starting at 1800 UTC evidence of a cold bias from deeper convection is found in the Thompson scheme and becomes more pronounced at 1900 UTC where BT $<$ 240 K are more frequent. This bias pattern continues to the 2000 UTC time step. Griffin et al. (2017) found similar behavior when assessing output from the High-Resolution Rapid Refresh model.

b. *Composite-based evaluation of CI*

The differences in Figs. 3 and 4 begin to scratch the surface on possible organizational differences in the spatial cloud coverage between the observations and microphysical schemes. Previous

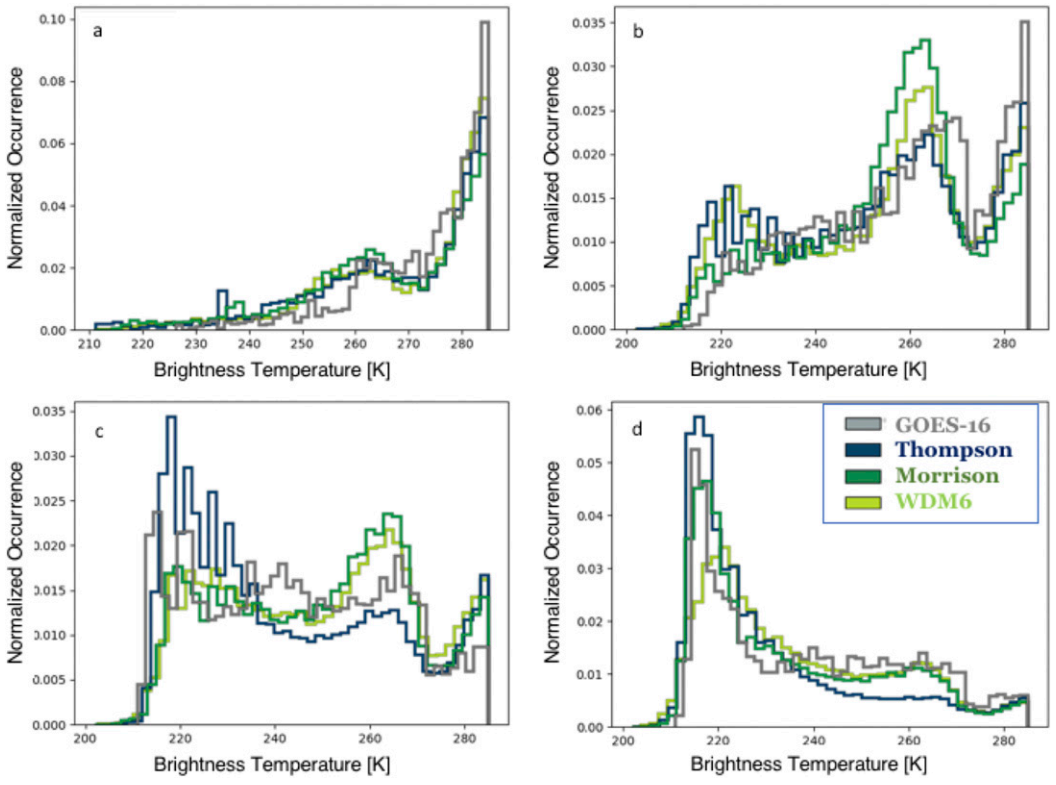

FIG. 4. Normalized ABI 10.35 μm brightness temperature probability density functions at (a) 1700, (b) 1800, (c) 1900, and (d) 2000 UTC. Brightness temperatures are binned every 2 K for *GOES-16* (gray) observations and Thompson (blue), Morrison (green), and WDM6 (light green) simulations.

studies have investigated cloud-top BT biases through matching cloud objects spatially and temporally to verify CI forecasts (e.g., Burghardt et al. 2014) or by implementing object-based analysis to track cloud systems to assess characteristics beyond point-by-point analysis (e.g., Griffin et al. 2017). However, these evaluations lack validation of the model representation of the cloud evolution characteristics leading to CI itself. The differences in Fig. 3 illustrate a direct overestimate of CI frequency during the model forecasts, but it is difficult to distinguish the mechanisms leading to this from domain-based or system-based statistics alone. Evaluation of CI processes based on the cloud life cycle is possible using composite strategies and allows investigation of simulated CI characteristics without the need to match with the observations in space and time. While this does not provide the same dichotomous validation when model objects are matched with observations in space and time, it allows evaluation of the full breadth of CI characteristics exhibited by the simulations.

To understand how clouds leading to CI evolve through time, the evolution of three satellite-based cloud-top interest fields will be described to characterize the changes in cloud-top growth and microphysical state. The 5-min temporal information content from the ABI sensor provides the opportunity for observing growth closer to cloud scales (e.g., Gravelle et al. 2016; Senf and Deneke 2017) when evaluating the model simulations. The satellite-based interest fields are derived using three BT-based methods that represent the cloud-top height using the 10.35 μm BT, 10.35 μm BTs cloud growth tendency at 5-min intervals, and cloud-top glaciation using 8.4–10.35 μm BT differences. Figures 6 and 7 provide box-and-whisker plots for cloud growth CI interest fields that detail the distribution of cloud-top BTs for time steps 15 min before and after CI is observed (time lag = 0 at CI).

Similar to clouds observed in Mecikalski et al. (2013), the 10.35 μm BTs begin near 270 K 15 min before CI occurs and continually cool (grow vertically) throughout the period (Fig. 6). For the Thompson and Morrison schemes, clouds 15 min before CI are warmer (shallower) compared to the ABI observed ranges. The median BTs from the Thompson and Morrison schemes move toward the *GOES-16* ABI median values over time resulting in increased cooling rates before CI occurrence (Fig. 7). In Fig. 7, the growth rates exhibit similar characteristics to the 5-min analysis in Senf and Deneke (2017), where the maximum cooling rates occur near CI and then the cloud-top cooling rate decreases afterward. The Morrison scheme displays faster growth rates 10–15 min before CI and the Thompson scheme exhibit a larger increase in cloud growth 5-min before CI. Further, all of the WRF Model simulations exhibit large ranges in BTs compared to the observed ABI clouds particularly after CI occurs. The model simulations produce a higher fraction of clouds that begin to warm, or slow in growth, after CI is detected (Fig. 7), suggesting cloud growth

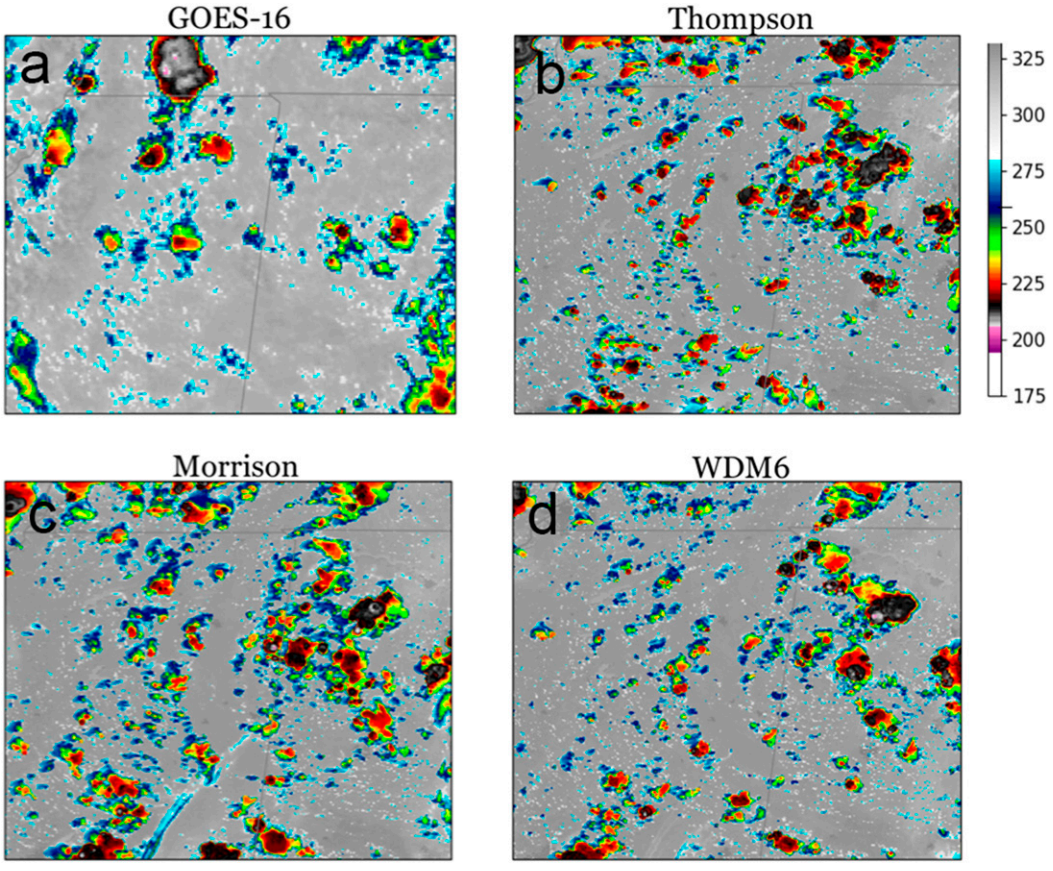

FIG. 5. Observed and simulated ABI 10.35 μm brightness temperatures (K) at 1900 UTC for (a) *GOES-16*, (b) Thompson, (c) Morrison, and (d) WDM6.

has ceased. When tracking the clouds through time, the CI cases from the Morrison simulation last no more than 20 min 42% of the time after CI was detected, whereas 35% of the CI cases in the Thompson simulation last 20 min or less, which suggests a higher number of congestus clouds compared to longer-lived deep cumulonimbus clouds in the Thompson and Morrison simulations. Mean values for the observed and simulated values are shown in Table 3 using the IQR, defined as the 25%–75% quartiles of the data in Figs. 6 and 7. The differences described above are also evident in Table 3, where higher growth rates before CI and a switch toward positive (warming) after CI are found in the Thompson and Morrison schemes.

There is a clear disconnect in the cloud development in the WDM6 microphysics that leads to a delay in CI detection resulting in colder cloud tops (Fig. 6; light green bars). While the WDM6 cloud growth rates in Fig. 7 exhibit a similar pattern as the Thompson and Morrison schemes, cloud heights in Fig. 6 are higher (colder), demonstrating that CI is detected later in the cloud life cycle compared to the other simulations. To further investigate cloud growth in the WDM6 simulation, the cloud evolution is plotted starting an additional 30 min before CI was detected (hatched bars in Figs. 6 and 7), which is the time step the median WDM6 10.35 μm BTs best match the ABI observations. The 30-min lagged WDM6 10.35 μm BTs in Fig. 6 more closely resemble the ABI observations, but the growth rates in Fig. 7 no longer exhibit the maximum cooling at time step zero originally found in both the *GOES-16* observations and simulated clouds. Instead, the lagged WDM6 evolution is more linear. The WDM6 scheme typically produces rain drop sizes that are too small (Morrison et al. 2015; Johnson et al. 2016; Lei et al. 2020). Radar reflectivity is proportional to the sum of the sixth power of the diameter; therefore, smaller drop size distributions will lead to lower reflectivities in the growing convection. Further, previous research describes the need for a glaciation-driven latent heat boost within clouds to elevate them toward CI (e.g.,

TABLE 2. The 10th percentile of the 10.3 μm BT distributions for the *GOES-16* observations and Thompson, Morrison, and WDM6 simulations at 1700, 1800, 1900, and 2000 UTC.

	1700	1800	1900	2000
GOES-16	257.6	241.2	228.6	217.5
Thompson	256.3	237.8	223.1	214.8
Morrison	254.5	240.3	229.6	216.5
WDM6	260.1	241.5	227.8	218.4

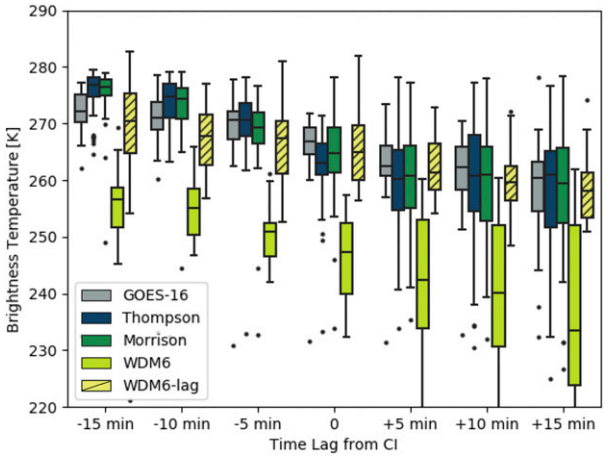

FIG. 6. Box-and-whisker plots of ABI 10.35 μm brightness temperatures (K) for *GOES-16* (gray), Thompson (blue), Morrison (green), WDM6 (light green), and WDM6 lagged 30 min (hatched). Bars are spaced at 5-min intervals with time = 0 defined as the time CI was detected.

Zipser 2003; Mecikalski et al. 2016b; Senf and Deneke 2017). The results from the cloud-top BTs indicate that the WDM6 scheme likely has a lag in rain growth and cloud glaciation that produces the added midtropospheric latent heating needed to reach CI, and subsequent large enough hydrometeors to produce a radar echo greater than 35 dBZ.

Direct comparison of BT channels sensitive to cloud-top microphysical changes and glaciation help shed light on how accurately the microphysics schemes handle ice processes in the top levels of the cloud (e.g., Mecikalski et al. 2010; Senf and Deneke 2017). Figure 8 displays box-and-whisker plots for the observed and simulated 8.4–10.35 μm BT differences. Due to

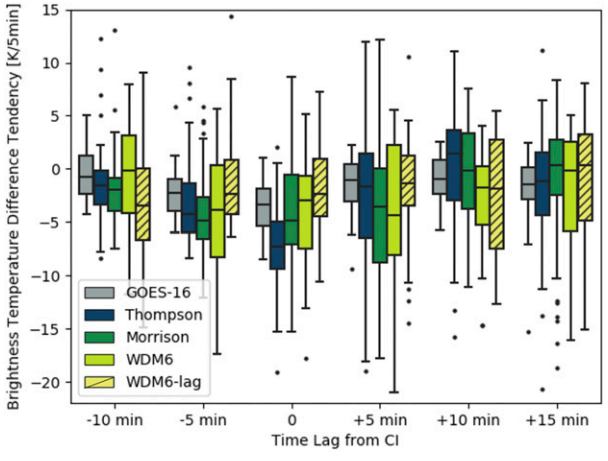

FIG. 7. Box-and-whisker plots for the ABI 10.35 μm brightness temperature growth tendency field for *GOES-16* (gray), Thompson (blue), Morrison (green), WDM6 (light green), and WDM6 lagged 30 min (hatched). Bars are spaced at 5-min intervals with time = 0 defined as the time CI was detected. Each tendency is the change in BT between the listed time step and the time step before.

TABLE 3. Differences of the mean BT (model − obs) of the 10.35 μm BT and 8.4–10.35 μm BT tendency computed using the mean of the interquartile range. Differences are given for time steps before and after CI is detected. All units are in K.

Time lag from CI (min)	Thompson	Morrison	WDM6	WDM6-lagged
		10.35 μm		
−15	3.45	3.28	−16.23	−1.51
−10	2.78	2.03	−16.31	−3.81
−5	0.34	−1.1	−20.02	−3.73
0	−3.48	−1.98	−19.93	−2.41
+5	−2.65	−2.61	−20.67	−0.61
+10	−1.33	−1.95	−23.52	−2.91
+15	−0.35	−1.13	−24.02	−2.52
		10.35 μm tendency		
−10	−1.16	−1.65	−2.65	−2.12
−5	−1.66	−2.39	0.55	−2.41
0	−3.96	−0.95	1.11	−1.72
+5	−0.88	−1.45	−0.14	−0.65
+10	1.75	0.75	−1.63	−1.04
+15	0.47	1.76	1.39	0.14

the different optical properties between liquid and ice, the BT difference switches from negative (below −2 K) for optically thick liquid clouds toward positive when the cloud top becomes fully glaciated (Baum et al. 2000). The observed BT difference from *GOES-16* shows that the clouds start as fully liquid 15 min before CI and then the BT difference trends toward less negative values thereafter, plateauing near −1 K. Baum et al. (2000) describe how positive trends in this BT difference field are driven by the presence of larger ice and liquid particles at cloud top. The larger particle size leads to smaller BT differences, and suggests that a mixed phase state is possible at cloud top in the *GOES-16* observations after CI is detected. Some clouds do exhibit positive BT differences; however, they are beyond the box-and-whisker ranges.

The three WRF bulk microphysical schemes are characterized by different evolutions of cloud-top glaciation BT differences (Fig. 8). The Thompson scheme has the closest pattern to observations with clouds starting around –2 K 15 min before CI and converging to a BT difference near −0.5 K at CI. The majority of cloud tops contain a negative BT difference in the Thompson simulation with a few switching to positive 15-min after CI detection. The Morrison scheme more efficiently converts from liquid to ice phases, and the glaciation trend increases monotonically before and after CI. Cloud-top glaciation is found in clouds starting at time-lag zero and the amount of cloud tops with positive BT differences increases monotonically until the majority of clouds are glaciated 15 min after CI. Similar to the observations and the Thompson scheme, the WDM6 simulation BT differences plateau after CI, but due to the delay in CI detection, clouds exhibit ice glaciation before CI detection. Using the 30-min lagged WDM6 BTs described above, the glaciation BT differences resemble the Thompson and observed *GOES-16* trend but continues to grow linearly. The presence of ice likely demonstrates that larger liquid precipitation hydrometeors are absent

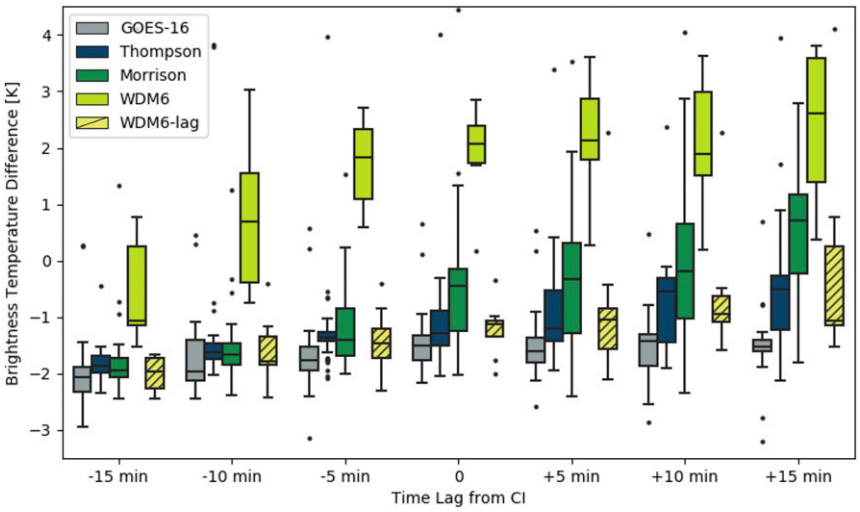

FIG. 8. As in Fig. 6, but for showing ABI 8.4–10.35 μm brightness temperature differences (K).

in the early WDM6 development, thereby delaying the detection of CI.

To examine differences in the evolution of in-cloud microphysics, Fig. 9 presents vertical profiles of liquid and frozen cloud mixing ratios for each simulation from 5 min before until 10 min after CI is detected. To provide additional insight into the behavior of the WDM6 scheme, the bottom row shows vertical profiles for the cloud mixing ratios from 25 to 10 min preceding CI. For all of the microphysics schemes, CI detection is coincident with the emergence of a precipitating core near 4–5 km and the formation of graupel near the cloud top. The WDM6 simulation contains a similar rain mixing ratio profile 5 min before CI when compared to the Thompson and Morrison simulations. In the WDM6 simulation, the delay in CI detection leads to more cloud water lofted to the upper levels along with higher mixing ratios for frozen hydrometers. For WDM6, the emergence of rain mixing ratios does not occur until 10 min before CI detection. Starting 25 min before CI cloud mixing ratios are still located well above the freezing level. Near 15 min before CI, small amounts of cloud ice and snow occur before the emergence of rain in the WDM6 simulation and the cloud continues to grow with cloud mixing ratios located as high as 10 km above the surface. This is consistent with the large cold biases in 10.35 μm BTs in Fig. 6 and Table 3. Both the WDM6 and Morrison schemes produce larger amounts of graupel and snow after CI leading to the positive BT difference bias shown in Fig. 8. The Thompson scheme still produces graupel in the upper levels of the cloud but is more efficient at producing rain at the surface. This leads to less ice aloft and the development of a plateau in the 8.4–10.35 μm BT differences after CI in the Thompson simulation and *GOES-16* observations; the 8.4–10.35 μm BT differences plateau in the Thompson simulation centered on –1, verifying the lack of cloud-top glaciation.

c. *CI processes related to cloud growth*

The WRF simulations contain more CI cloud objects than observed, where the Thompson and Morrison simulations have the most cloud objects reaching CI. As shown in Fig. 7, after CI is detected, the simulated clouds have a large spread in growth rates. The *GOES-16* observed BT histograms presented in Fig. 4 are characterized by 10.35 μm BT peaks near 260 and 220 K signifying that the CI cloud objects are subset into shallower precipitating congestus clouds with warmer cloud tops and clouds that continue to grow into deep cumulonimbus clouds. The 35 dBZ threshold used to define CI in this case study captures precipitating clouds within the 10.35 μm 260 and 220 K cloud subsets. These clouds all reach CI and likely produce significant precipitation; however, combining the two subsets of cloud growth can lead to ambiguity when comparing the model and observational differences.

To investigate the cloud characteristics associated with the varying life cycles of cloud growth, the CI definition is modified to discriminate both sets of clouds. The cloud evaluation will partition CI cloud objects into those reaching 10.35 μm BTs $<$ 250 K at some point in their life cycle and those with cloud-top BTs remaining warmer than 250 K. The 250 K threshold was chosen using the BT histograms in Fig. 4, and since the clouds observed by *GOES-16* reaching 250 K demonstrate continuous growth after CI. For convenience, we will refer to cloud objects reaching the 250 K threshold as the ''cold-CI cloud'' category and cloud objects remaining warmer than 250 K as the ''warm-CI cloud'' category. The 250 K threshold will be applied to the observed and simulated CI cloud objects. The warm- and cold-CI clouds from the WRF simulations will be further subset by the top 50% of cloud objects in each category that most closely match the observed *GOES-16* observed growth rates after CI is detected. Cloud objects outside the top 50% best matching *GOES-16* growth rates illustrate simulated cloud objects where growth is outside the ranges measured by the *GOES-16* observations. Because the temporal delay for CI events in the WDM6 simulation leads to a limited number of cases where cloud-top BTs remain warmer than 250 K, this analysis will focus on the Thompson and Morrison simulations only.

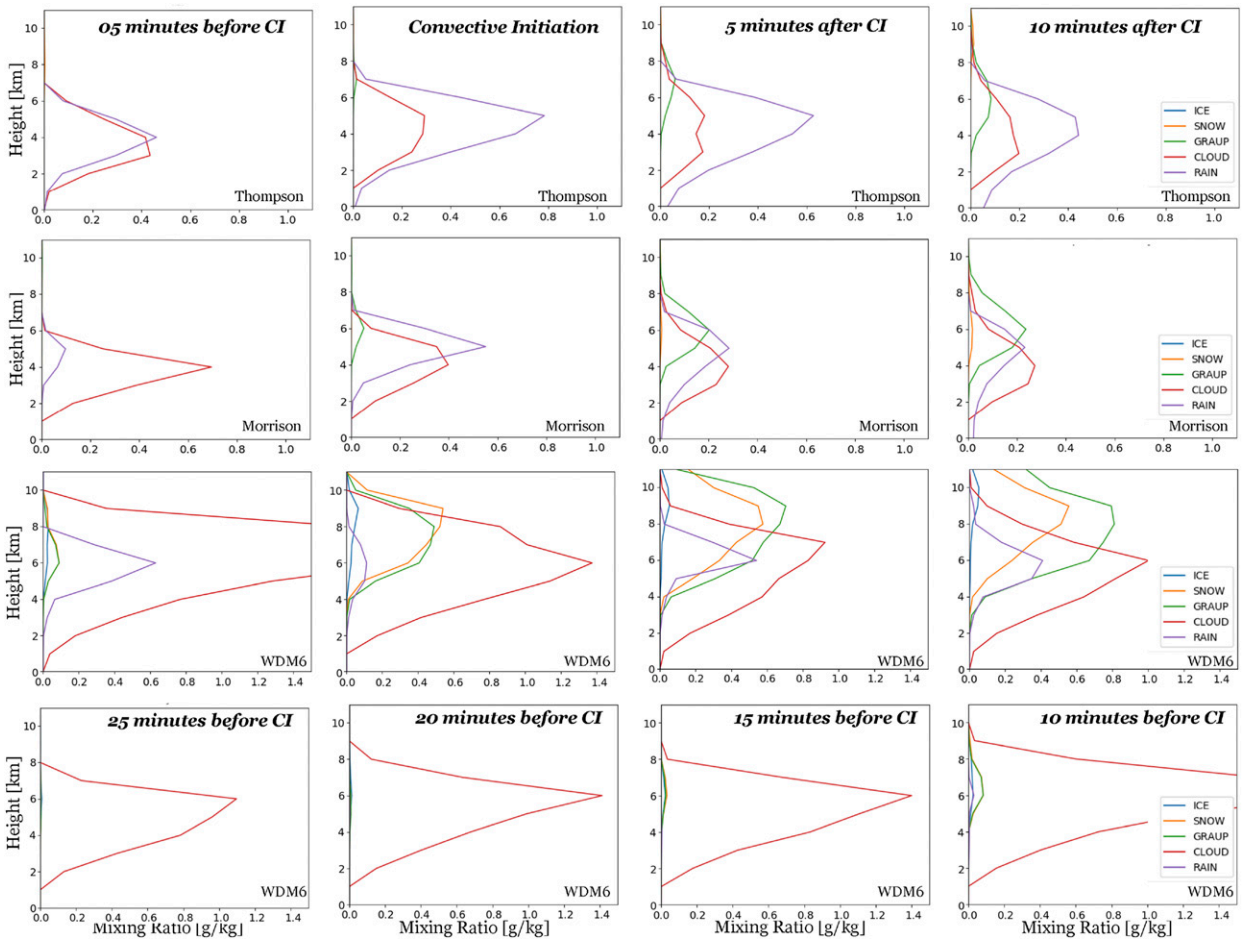

FIG. 9. Evolution of mean profiles for ice, snow, graupel, cloud water, and rainwater mixing ratios from 5 min before CI until 10 min after CI was identified. Profiles are shown for (top) Thompson, (second row) Morrison, and (bottom two rows) WDM6 bulk microphysics schemes. The bottom row contains WDM6 profiles lagged an additional 20 min.

Table 4 provides a summary of the total CI cloud objects tracked when CI clouds are separated into warm-CI and cold-CI cloud cases. It is evident that the overestimation of simulated cloud objects reaching 35 dBZ is due to an increase in warm-CI clouds with 21, 75, and 84 warm-CI clouds from *GOES-16* observations, Thompson, and Morrison, respectively. The Thompson and Morrison schemes produce 46 and 54 cloud objects reaching 250 K, respectively. Though this is still higher than the 31 objects observed by *GOES-16*, it does lead to a better match than when using the 35 dBZ CI definition alone.

The resulting 10.35 μm cloud-top BTs and BT growth rate tendencies using the warm- and cold-CI cloud categories are displayed in Figs. 10 and 11. Separating the CI cloud objects into warm and cold categories leads to a clear difference in the 10.35 μm cloud-top heights in Fig. 10. Near the time CI is detected, the observed and simulated warm-CI cloud growth halts and the 10.35 μm BTs remain nearly constant (Fig. 10a). This is consistent with the warm-CI clouds BT tendency where most clouds observed by *GOES-16* display zero tendency and both sets of simulations warm after CI detection resulting in positive BT tendencies (Fig. 11a). On the other hand, there is a clear deepening in the cold-CI clouds after CI as the 10.35 μm BT continues to decrease (Fig. 10b). The cloud-top BTs for cold-CI clouds are well below the freezing level of 273 K at the time CI is detected. The cloud-top BTs in Fig. 10 and

TABLE 4. Number of total cloud objects with 10.35 μm brightness temperature < 285 K, number of CI cloud objects meeting the 35 dBZ criterion, number of CI cloud objects meeting the 35 dBZ and 250 K criterion, and the number of CI cloud objects meeting the 35 dBZ criterion but not the 250 K criterion. Results are shown for the *GOES-16* observations and the Thompson and Morrison simulations.

	Total cloud objects BT < 285 K	Cloud objects with dB$Z \geq 35$	Cloud objects reaching 250 K	Cloud objects that do not reach 250 K
GOES-16	546	52	31	21
Thompson	1853	121	46	75
Morrison	2160	136	52	84

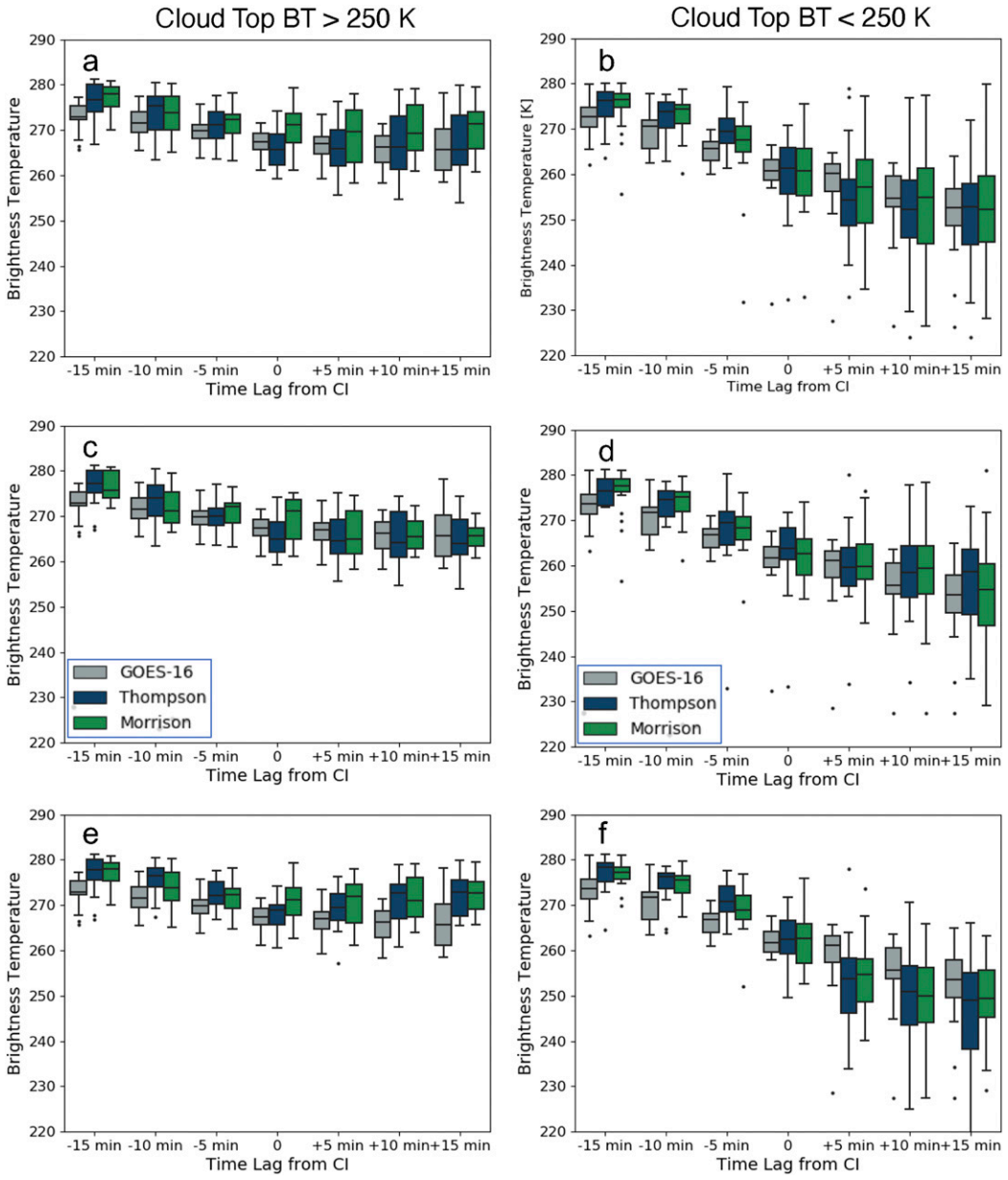

FIG. 10. As in Fig. 6, but for cases subset into warm-CI clouds and cold-CI clouds. (left) Warm-CI clouds for (a) all cases, (c) top 50% best-matched cases, and (e) cases outside 50% best matched. (right) Cold-CI clouds for (b) all cases, (d) top 50% best-matched cases, and (f) cases outside 50% best matched. Results are shown for the Thompson (blue) and Morrison (green) simulations.

tendencies in Fig. 11 for the cold-CI cases resemble cloud-top BT trends described in Matthee and Mecikalski (2013) who demonstrated that rapidly growing convection [growth rates ~10°C (15 min)$^{-1}$] are more likely to produce heavy rain and lightning compared to CI cases with slower growth.

Comparing the top 50% of simulated cloud objects most closely matching the observed *GOES-16* growth rates for warm and cold-CI clouds naturally leads to improvement for both cloud height and growth rates within the best matched cases. For these clouds, median cloud growth rates become closer to observations and the spread in 10.35 μm BT and BT growth rates (Figs. 10c,d and 11c,d) after CI detection are greatly reduced. The 10.35 μm cloud-top BTs in the simulations remain consistently warmer than *GOES-16* before CI detection leading to the same pattern of increased growth rates for Thompson cloud objects shown previously in Fig. 7. The Morrison cloud objects display increased growth rates 10 min before CI in the warm-CI cases in Fig. 11a, but growth rates closer to *GOES-16* occur afterward. The simulated warm-CI cloud cases outside the top 50% best-matching *GOES-16*

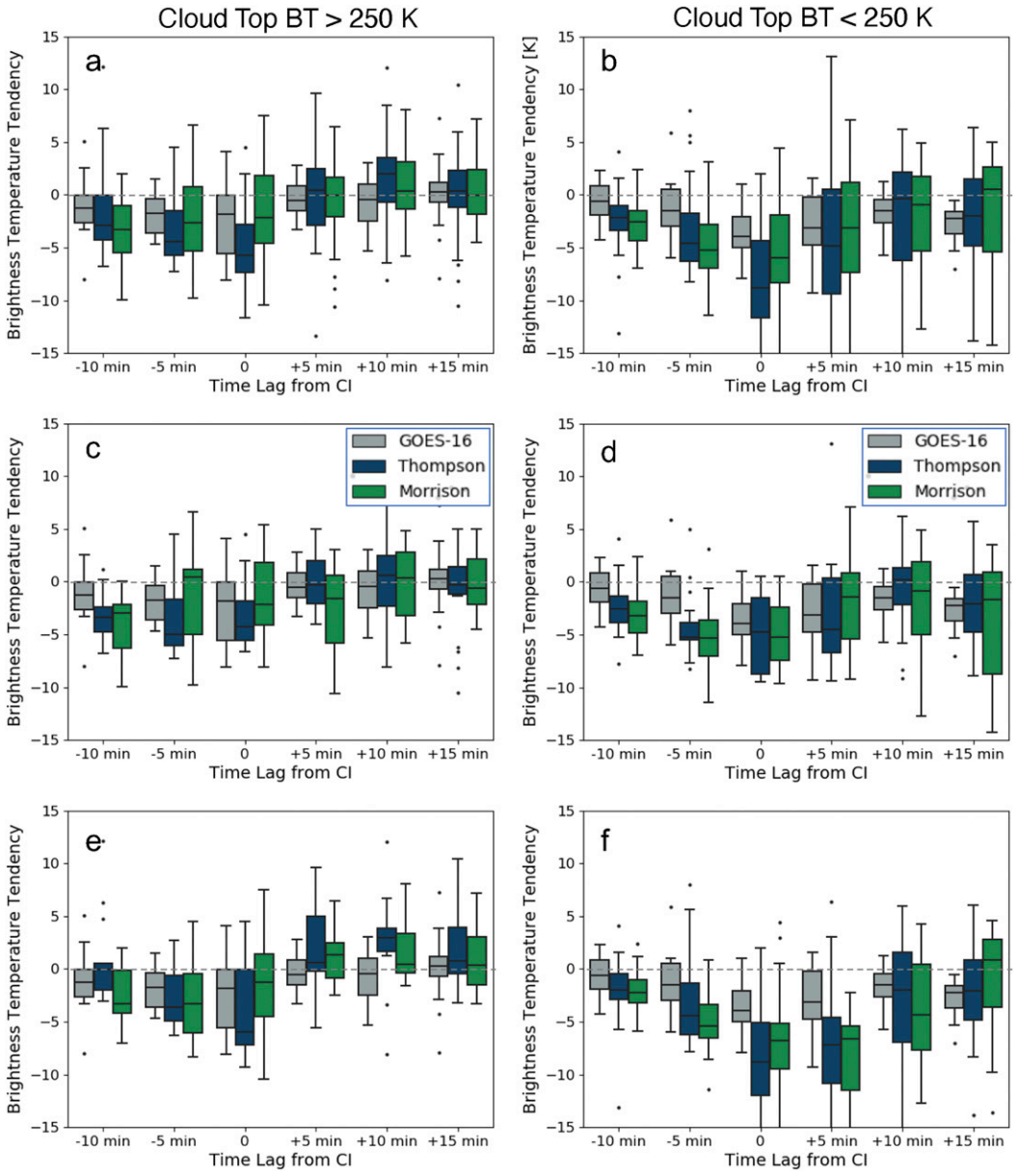

FIG. 11. As in Fig. 7, but for cases subset into warm-CI clouds and cold-CI clouds. (left) Warm-CI clouds for (a) all cases, (c) top 50% best-matched cases, and (e) cases outside 50% best matched. (right) Cold-CI clouds for (b) all cases, (d) top 50% best-matched cases, and (f) cases outside 50% best matched. Results are shown for the Thompson (blue) and Morrison (green) simulations.

observed growth in Figs. 10e and 11e show signs of decay quickly after CI is detected where cloud growth trends are warmer than the observations, whereas the simulated cold-CI cloud cases in Figs. 10f and 11f display rapid growth at CI detection and 5 min after CI. It is interesting to note that the warm-CI cloud objects contain cloud growth rates that are similar to the cold-CI clouds before and at CI detection. This suggests that in the early stages of CI, the BT interest fields used to forecast CI might not be able to differentiate clouds with sustained growth from those that decay. This scenario could lead to false positives in geostationary satellite–based severe storm nowcasting algorithms since early cumulus cloud growth signatures are not always associated with CI events in the coming 30–45 min (Mecikalski and Bedka 2006).

Figure 12 uses 8.4–10.35 μm BT differences to evaluate signals in cloud-top glaciation in the warm-CI and cold-CI cloud categories. For warm-CI clouds, the WRF simulated BT differences closely track the observations, where the clouds start as fully liquid 15 min before CI and then the BT difference trends toward less negative values thereafter, plateauing just above -2 K. For the cold-CI clouds, the *GOES-16* observed BT difference are closer to zero; however, negative values

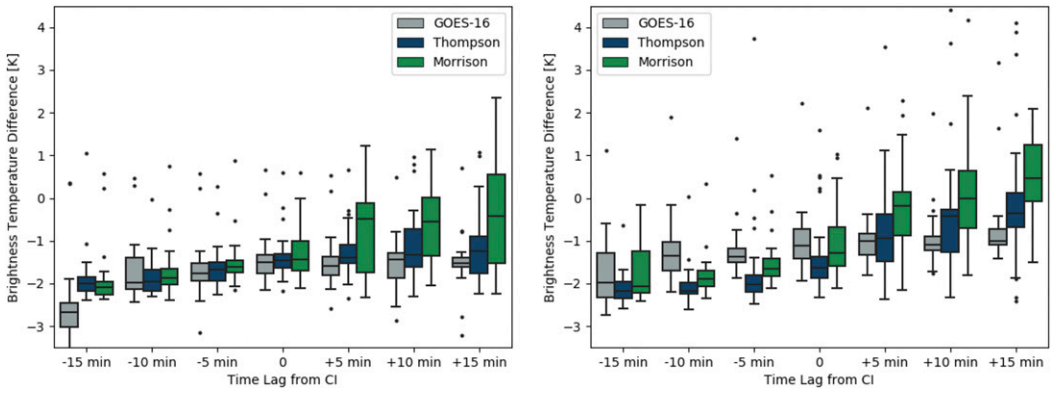

FIG. 12. The ABI 8.4–10.3 μm BT difference to evaluate cloud-top glaciation for cases subset into (left) warm-CI clouds and (right) cold-CI clouds. Results are shown for the Thompson (blue) and Morrison (green) simulations.

before and after CI indicate a cloud top that is not fully glaciated. A slight positive trend occurs in observed cold-CI cloud BT differences proving evidence that cloud-top microphysics contain larger hydrometeor sizes or ice after CI, which does not occur in warm-CI clouds. A larger number of outliers occur above zero for the observations and simulations indicating that more clouds have reached a fully glaciated state in the cold-CI category. For both microphysics schemes, the simulated cloud BT differences are nearly constant until 5 min before CI, thereby demonstrating a possible delay in the presence of ice or larger liquid hydrometeors near the cloud top compared to observations. At CI detection, BT differences for both microphysics schemes begin to quickly move toward more positive values and display evidence of a glaciated cloud top 15 min after CI. This positive BT difference also exists in the Morrison scheme for warm-CI clouds, providing further evidence of an overestimation of cloud ice after CI.

Figure 13 compares mean mixing ratio profiles for the warm- and cold-CI cloud categories. Differences are evident at the time when CI is detected, where the Thompson scheme more efficiently produces rain hydrometeors than the Morrison scheme. There is also a discernable difference between the warm-CI and cold-CI clouds, where mixing ratios from the cold-CI clouds are consistently larger than occurred during the warm-CI cloud objects. For example, profile maxima in cloud water mixing ratios remain higher in the cold-CI clouds. This sustained cloud water source likely aids the creation of rain, graupel, and other ice hydrometeors, but it is difficult to fully evaluate how the mixing ratios are impacting growth due to the differences in mixing ratios between the microphysics schemes.

Figure 14 displays cloud mixing ratio tendency profiles for cloud objects in the warm-CI and cold-CI cloud categories. Cold-CI cloud objects are further separated into the best matched cloud objects and cloud objects that experience more rapid growth described in Fig. 10. All warm-CI cloud objects are combined as the tendency profiles are similar. The tendency profiles were created by differencing each 5-min interval with the time step before it for each cloud object and then

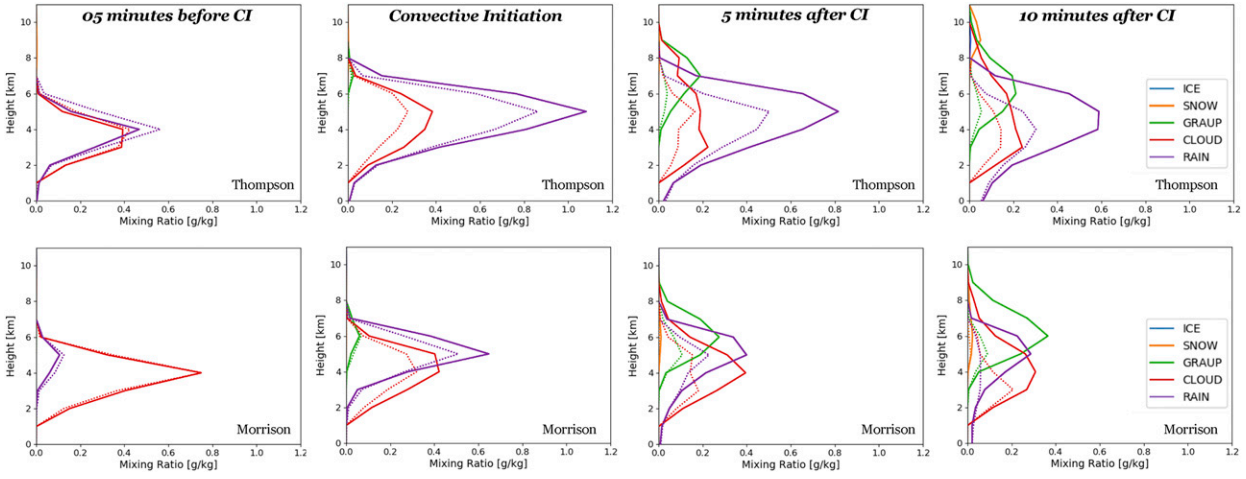

FIG. 13. Evolution of mean profiles for ice, snow, graupel, cloud water, and rainwater mixing ratios from 5 min before CI until 10 min after CI was identified. Profiles are shown for (top) Thompson and (bottom) Morrison simulations for cold-CI clouds (solid lines) and warm-CI clouds (dotted lines).

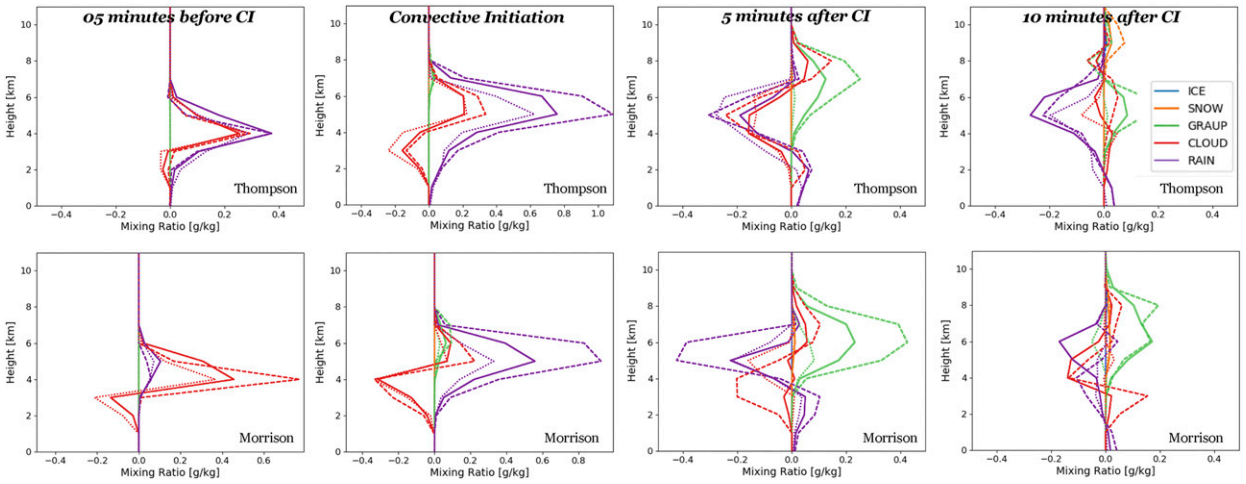

FIG. 14. Evolution of mean in cloud tendency profiles of ice, snow, graupel, cloud water, and rainwater mixing ratios from 5 min before CI until 10 min after CI was observed. Profiles are shown for the (top) Thompson and (bottom) Morrison simulations. The growth categories are shown for warm-CI clouds (dotted lines), best-matched cases cold-CI clouds (solid lines), and growth cold-CI clouds (dashed line).

averaged. The tendency profiles exhibit better agreement between the microphysics schemes and are able to describe how changes in cloud microphysics could impact the growth of the cloud. The mixing ratio tendency profiles for the warm-CI and cold-CI cloud categories are similar before CI is detected, particularly in the Thompson scheme. In Fig. 13, increases in rain mixing ratios in the simulated clouds develop near 4 km in the time step before CI detection. This increase of rain hydrometeors leads to CI detection 5 min later. Five minutes before CI, there is an discernable difference in the cloud water fluxed from the lower-levels of the cloud to the upper levels, where the best-matched and rapid-growth cold-CI clouds lose less cloud water compared to the warm-CI clouds. Cloud water is gained near 4 km for the warm-CI clouds, best-matched cold-CI clouds, and rapid-growth cold-CI clouds, but less cloud water is lost below 3 km where a smaller negative cloud water tendency occurs in cold-CI cloud categories. This tendency occurs at the CI time step as well.

At time-lag zero when CI is detected, both microphysics schemes show increases in rainwater mixing ratios throughout the depth of the cloud, which monotonically increases as a function of growth and the development of graupel occurs between 6 and 8 km. Five minutes after CI is detected, the sustained cloud water in the lower levels of the cloud leads to higher rain mixing ratios and a monotonic increase in graupel from warm-CI clouds to the cold-CI clouds, which is found in both of the microphysics schemes. This helps confirm previous geostationary-based assessments (e.g., Mecikalski et al. 2016a,b; Senf and Deneke 2017) that suggest growth related to CI is aided by latent heat release from ice formation near and below cloud top. Figure 13 also shows that the process requires sustained latent heating in the lower levels from condensation, which was also shown to be the case when 1-min-resolution *GOES-14* data were used to analyzing cumulus clouds undergoing the CI process (Mecikalski et al. 2016b). For the warm-CI clouds in Fig. 13, the larger loss of cloud water in the lower levels of the clouds leads to lower rain and graupel mixing ratios with negative tendencies for all cloud species above 4 km 10 min after CI was detected. Thus, clouds lacking the sustained source of low-level cloud water are unable to sustain their growth over time.

Due to the warm and moist boundary layer found in the southeastern United States the warm (>0°C) portion of the cloud is 3–4 km deep (Fig. 9), and accurate representation of warm rain processes are essential for CI in weakly forced environments over this region. Combined radar and geostationary satellite studies have demonstrated that heavily raining convection with similar glaciation BT differences found in Figs. 8 and 12 typically contain weaker updrafts and lower ice contents at the cloud top (e.g., Mecikalski et al. 2013; Matthee et al. 2014; Senf and Deneke 2017) compared to lightning producing storms; therefore, warm rain processes are a likely pathway to make a 35 dBZ echo for both the warm-CI clouds and cold-CI clouds. Early rain formation dictated by the autoconversion process varies between the microphysics schemes resulting in the differences found in Fig. 13 and resulting ice aloft in the cloud (e.g., Bao et al. 2019). The ABI comparisons in Figs. 10 and 11 help demonstrate that the simulations can replicate the evolution in CI BT signatures. The comparisons of the BT differences associated with cloud phase provide evidence that the Morrison scheme produces too much graupel in the best-matched cases (Fig. 14). While the Thompson scheme best matches the observed 8.4–10.35 μm BT difference for this case study for both warm- and cold-CI clouds, further evaluation assessing the sensitivity of the CI processes with land surface models and planetary boundary layer schemes will be needed.

5. Discussion and conclusions

In this study, the characteristics of simulated convection leading to CI from different bulk cloud microphysics schemes

are assessed using version 3.9.1.1 of the WRF Model. The study examined the evolution of cloud objects associated with CI for a case study from 20 May 2018 where weakly forced convection occurred over parts of Mississippi and Alabama that eventually lead to multiple reports of high wind and hail. Evaluating in this environment provides analysis where microphysics are the primary driver in pushing convection toward heavily precipitating convection. Three model sensitivity experiments employing 500 m horizontal grid spacing were completed where all model components were identical except for the cloud microphysics scheme. *GOES-16* ABI infrared BTs were simulated for each model experiment using the CRTM and then directly compared to *GOES-16* observed BTs using a lag-composite analysis, where time zero was defined as the time CI was detected. CI for the model and observations is defined as the first time a 35 dBZ radar echo occurred in the cloud column. Three BT-derived fields commonly used in CI nowcasting applications were compared between the models and observations to understand changes in cloud-top height, cloud growth rate, and hydrometeor phases over time.

In general, the WRF simulations were able to capture the general trend in cloud growth rates and cloud-top area over time when maximum cooling occurred near the time CI was detected. The simulations contain a larger spread of 10.35 μm BTs after the detection of CI. Furthermore, the number of clouds reaching CI is too frequent in all simulations due to a large number of convective cases reaching CI and then quickly decaying afterward. This pattern was most pronounced when using the Morrison scheme. For the Thompson scheme, around 35% of CI cases sustain 20 min or less after CI, whereas this increases to 42% in the Morrison scheme. Too-frequent convection could lead to issues when forecasting CI due to the prevalence of convection formation in raining outflow boundaries in the southeastern United States (Goggins et al. 2010). Delays in rain hydrometeor formation occur in the WDM6 bulk microphysics scheme, which led to a delay in the detection of CI compared to the *GOES-16* observations. This then caused a cold bias in the simulated 10.35 μm BTs > 20 K throughout the CI process when this scheme was used. Lagging the WDM6 BT time series by 30 min improved comparisons with the 10.35 μm cloud-top BTs, but cloud growth rates no longer exhibited the maximum growth at CI, likely due to the absence of ice growth at these time steps and thus lacking the upper-level latent heating needed to support cloud growth.

Evaluating the simulated clouds using BTs demonstrates the benefits of using high-resolution satellite observations to examine cloud processes using model simulations. It also provides a platform to deconstruct cloud properties leading to trends in CI properties. When partitioning the results into warm-CI and cold-CI clouds the simulated CI cases produce a range of 10.35 μm cloud-top BTs more akin to the *GOES-16* observations. Although differences in microphysical processes are evident, comparison of the tendencies in mixing ratio profiles from these two microphysics schemes reveals agreement in the tendency of in-cloud mixing rations related to convection initiation and cloud growth. Cold-CI clouds are characterized by an increase in cloud water at lower levels near the time of CI that is then lofted to the upper portion of the cloud, whereas warm-CI clouds contain less cloud water at CI. Increased cloud water in the upper levels contributes to an increase in graupel formation near cloud top, which corresponds to the times of maximum growth and helps confirm that ice formation is a necessary component in CI and cloud growth leading to longer lasting storms. This also indicates that sustained condensation in the lower levels of the cloud is necessary to provide sustained sources of cloud water to be lofted into the upper portion of the convective clouds.

Using the 8.4–10.35 μm BT differences, observed changes in *GOES-16* cloud-top phase in CI events yield a positive BT difference trend that plateaus shortly after CI. The observed *GOES-16* BT does not reach full cloud-top glaciation (BT differences remain < 0), but the positive trend provides evidence of the onset of ice and larger hydrometers at the cloud top. The CI cases from the Thompson microphysics scheme yield a similar result, whereas the Morrison and WDM6 schemes are too efficient at creating cloud ice particles (specifically graupel) and a glaciated cloud top (8.4–10.35 μm BT difference switches to positive). Inspection of in-cloud mixing ratio profiles reveals that the Thompson scheme more readily converts cloud water to precipitation, whereas the Morrison scheme is able to loft more cloud water to higher levels, leading to increased graupel formation. When comparing cold-CI and warm-CI clouds, the cold bias from the Morrison scheme remains providing further evidence that it is producing too much graupel near the cloud top.

The application of observation-based CI techniques present a novel methodology to evaluate high-resolution models with satellite data and examine the processes leading to CI development. The results from this study illustrate that the model simulations are able represent cloud evolution, but warm-CI clouds are too frequent. Previous radar-based studies that demonstrate cloud tops with lower ice contents, such as those observed in the *GOES-16* ABI BT signatures (Fig. 8), contain weaker updrafts (e.g., Matthee et al. 2014; Senf and Deneke 2017), which suggests radar reflectivity due to warm rain. The lower-level condensational growth and warm rain processes are important for CI as early rainwater partitioning in bulk microphysics can impact downstream graupel production. Further, small rain hydrometeors have been found in WDM6 using dual-polarized radar comparisons (e.g., Johnson et al. 2016; Lei et al. 2020), which affects timing of CI detection. Bao et al. (2019) illustrate that differences in autoconversion parameterizations early in warm rain development can lead to downstream differences in graupel production. The delay in rain formation in the WDM6 simulation and the increased graupel formation when using the Morrison scheme suggests that insight into differences within autoconversion parameterizations could help sort differences in cloud evolution. Further analysis comparing simulated cloud growth with clouds best matching *GOES-16* observations could help refine which autoconversion rates are accurate in the cloud microphysics schemes. The Thompson scheme most accurately describes the ice mixing ratios reaching cloud top at the time of CI, but all of the parameterization schemes generally produce cloud tops that are too warm early in development, thereby leading to higher growth rates before CI.

This is a single case study so additional case studies using satellite BTs and objected-based methods to evaluate the characteristics of CI may be necessary to reinforce these findings. Before CI was detected, IR BTs at cloud top were similar between warm-CI and cold-CI clouds in the WRF Model simulations. This suggests that information content from cloud-top properties alone, such as ones utilized in geostationary-based CI forecasting, may be insufficient when forecasting CI during the early stages of cloud development when the convection is weakly forced. Additional simulations shedding light on other factors controlling the growth of simulated convection will be useful to aid in understanding the conditions optimal for CI growth in weakly forced cases. Future studies could concentrate on how the use of land surface models and planetary boundary layer schemes impact convective growth, updraft characteristics, and latent heating leading to CI. Finally, utilizing observations from ground-based active sensors that provide high-resolution vertical profiles of hydrometeors and updrafts will be key in constraining model-based evaluations of convection. Such modeling studies are planned as well as observational analysis evaluating convective evolution using data from the Atmospheric Radiation Measurement (ARM) program matched to observed *GOES-16* CI cases.

Acknowledgments. The authors would like to acknowledge the support by NSF Grant AGS-1746119 to complete this work. Further, we thank Monica Harkey and Sarah Griffin from the University of Wisconsin for their support in WRF and CRTM development and Greg Thompson and Hugh Morrison at UCAR for useful conversations on microphysical evaluations. Finally, we thank the anonymous reviewers and editor for comments and suggestions that significantly improved the quality of this paper.

Data availability statement. GOES-16 data used in this analysis can be downloaded from the National Oceanic and Atmospheric Administration Amazon Web Services (NOAA AWS; https://registry.opendata.aws/noaa-goes) data inventory. Ground-based NEXRAD data can be downloaded from the National Climatic Data Center (https://www.ncdc.noaa.gov/data-access/radar-data). The authors have archived the WRF output data used in this study, as well as source codes for computing cloud positions, on a Space Science and Engineering server located at the University of Wisconsin. These files can be made available to anyone upon request.

REFERENCES

Apke, J. M., J. R. Mecikalski, K. Bedka, E. W. McCaul, C. R. Homeyer, and C. P. Jewett, 2018: Relationships between deep convection updraft characteristics and satellite-based super rapid scan mesoscale atmospheric motion vector–derived flow. *Mon. Wea. Rev.*, **146**, 3461–3480, https://doi.org/10.1175/MWR-D-18-0119.1.

Asefi-Najafabady, S., K. Knupp, J. R. Mecikalski, and R. M. Welch, 2012: Radar observations of mesoscale circulations induced by a small lake under varying synoptic-scale flows. *J. Geophys. Res.*, **117**, D01106, https://doi.org/10.1029/2011JD016194.

Bao, J., S. A. Michelson, and E. D. Grell, 2019: Microphysical process comparison of three microphysics parameterization schemes in the WRF model for an idealized squall-line case study. *Mon. Wea. Rev.*, **147**, 3093–3120, https://doi.org/10.1175/MWR-D-18-0249.1.

Baum, B. A., P. F. Soulen, K. I. Strabala, M. D. King, S. A. Ackerman, W. P. Menzel, and P. Yang, 2000: Remote sensing of cloud properties using MODIS airborne simulator imagery during SUCCESS. 2. Cloud thermodynamic phase. *J. Geophys. Res.*, **105**, 11 781–11 792, https://doi.org/10.1029/1999JD901090.

Borbas, E. E., R. O. Knuteson, S. W. Seemann, E. Weisz, L. Moy, and H.-L. Huang, 2007: A high spectral resolution global land surface infrared emissivity database. *Joint 2007 EUMETSAT Meteorological Satellite Conf. and the 15th Satellite Meteorology and Oceanography Conf. of the American Meteorological Society*, Amsterdam, Netherlands, EUMETSAT, P.50, https://www.ssec.wisc.edu/meetings/jointsatmet2007/pdf/borbas_emissivity_database.pdf.

Browning, K. A., and D. Atlas, 1965: Initiation of precipitation in vigorous convective clouds. *J. Atmos. Sci.*, **22**, 678–683, https://doi.org/10.1175/1520-0469(1965)022<0678:IOPIVC>2.0.CO;2.

Burghardt, B. J., C. Evans, and P. J. Roebber, 2014: Assessing the predictability of convection initiation in the high plains using an object-based approach. *Wea. Forecasting*, **29**, 403–418, https://doi.org/10.1175/WAF-D-13-00089.1.

Bytheway, J. L., and C. D. Kummerow, 2015: Toward an object-based assessment of high-resolution forecasts of long-lived convective precipitation in the central U.S. *J. Adv. Model. Earth Syst.*, **7**, 1248–1264, https://doi.org/10.1002/2015MS000497.

——, and ——, 2018: Consistency between convection allowing model output and passive microwave satellite observations. *J. Geophys. Res. Atmos.*, **123**, 1065–1078, https://doi.org/10.1002/2017JD027527.

——, ——, and C. Alexander, 2017: A features-based assessment of the evolution of warm season precipitation forecasts from the HRRR model over three years of development. *Wea. Forecasting*, **32**, 1841–1856, https://doi.org/10.1175/WAF-D-17-0050.1.

Cancelada, M., P. Salio, D. Vila, S. W. Nesbitt, and L. Vidal, 2020: Backward Adaptive Brightness Temperature Threshold Technique (BAB3T): A methodology to determine extreme convective initiation regions using satellite infrared imagery. *Remote Sens.*, **12**, 337, https://doi.org/10.3390/rs12020337.

Cintineo, J. L., M. J. Pavolonis, J. M. Sieglaff, L. Cronce, and J. Brunner, 2020: NOAA ProbSevere v2.0—ProbHail, ProbWind, and ProbTor. *Wea. Forecasting*, **35**, 1523–1543, https://doi.org/10.1175/WAF-D-19-0242.1.

Cintineo, R., J. A. Otkin, M. Xue, and F. Kong, 2014: Evaluating the performance of planetary boundary layer and cloud microphysical parameterization schemes in convection permitting ensemble forecasts using synthetic *GOES-13* satellite observations. *Mon. Wea. Rev.*, **142**, 163–182, https://doi.org/10.1175/MWR-D-13-00143.1.

Ding, S., P. Yang, F. Weng, Q. Liu, Y. Han, P. van Delst, J. Li, and B. Baum, 2011: Validation of the community radiative transfer model. *J. Quant. Spectrosc. Radiat. Transfer*, **112**, 1050–1064, https://doi.org/10.1016/j.jqsrt.2010.11.009.

Fiolleau, T., and R. Roca, 2013: An algorithm for the detection and tracking of tropical mesoscale convective systems using infrared images from geostationary satellite. *IEEE Trans. Geosci. Remote Sens.*, **51**, 4302–4315, https://doi.org/10.1109/TGRS.2012.2227762.

Gambill, L. D., and J. R. Mecikalski, 2011: A satellite-based summer convective cloud frequency analysis over the southeastern United States. *J. Appl. Meteor. Climatol.*, **50**, 1756–1769, https://doi.org/10.1175/2010JAMC2559.1.

Goggins, G. D., M. L. Grantham, S. W. Unger, K. B. Laws, K. J. Pence, and L. Dawson, 2010: Analysis of summer convection over central Alabama. *15th Symp. on Meteorological Observation and Instrumentation*, Atlanta, GA, Amer. Meteor. Soc., 9.2, http://ams.confex.com/ams/pdfpapers/161408.pdf.

Grasso, L. D., and T. Greenwald, 2004: Analysis of 10.7-μm brightness temperatures of a simulated thunderstorm with two-moment microphysics. *Mon. Wea. Rev.*, **132**, 815–825, https://doi.org/10.1175/1520-0493(2004)132<0815:AOMBTO>2.0.CO;2.

Gravelle, C. M., J. R. Mecikalski, W. E. Line, K. M. Bedka, R. A. Petersen, J. M. Sieglaff, G. T. Stano, and S. J. Goodman, 2016: Demonstration of a GOES-R satellite convective toolkit to ''bridge the gap'' between severe weather watches and warnings: An example from the 20 May 2013 Moore, Oklahoma, tornado outbreak. *Bull. Amer. Meteor. Soc.*, **97**, 69–84, https://doi.org/10.1175/BAMS-D-14-00054.1.

Griffin, S. M., J. A. Otkin, C. M. Rozoff, J. M. Sieglaff, L. M. Cronce, and C. R. Alexander, 2017: Methods for comparing simulated and observed satellite infrared brightness temperatures and what do they tell us? *Wea. Forecasting*, **32**, 5–25, https://doi.org/10.1175/WAF-D-16-0098.1.

——, ——, G. Thompson, M. Frediani, J. Berner, and F. Kong, 2020: Assessing the impact of stochastic perturbations in cloud microphysics using *GOES-16* infrared brightness temperatures. *Mon. Wea. Rev.*, **148**, 3111–3137, https://doi.org/10.1175/MWR-D-20-0078.1.

Han, D., J. Lee, J. Im, S. Sim, S. Lee, and H. Han, 2019: A novel framework of detecting convective initiation combining automated sampling, machine learning, and repeated model tuning from geostationary satellite data. *Remote Sens.*, **11**, 1454, https://doi.org/10.3390/rs11121454.

Harris, R. J., J. R. Mecikalski, W. M. MacKenzie, P. A. Durkee, and K. E. Nielsen, 2010: The definition of GOES infrared lightning initiation interest fields. *J. Appl. Meteor. Climatol.*, **49**, 2527–2543, https://doi.org/10.1175/2010JAMC2575.1.

Helmus, J. J., and S. M. Collis, 2016: The Python ARM Radar Toolkit (Py-ART), a library for working with weather radar data in the Python Programming Language. *J. Open Res. Software*, **4**, e25, https://doi.org/10.5334/jors.119.

Hong, S.-Y., Y. Noh, and J. Dudhia, 2006: A new vertical diffusion package with an explicit treatment of entrainment processes. *Mon. Wea. Rev.*, **134**, 2318–2341, https://doi.org/10.1175/MWR3199.1.

Iacono, M. J., J. S. Delamere, E. J. Mlawer, M. W. Shephard, S. A. Clough, and W. D. Collins, 2008: Radiative forcing by long-lived greenhouse gases: Calculations with the AER radiative transfer models. *J. Geophys. Res.*, **113**, D13103, https://doi.org/10.1029/2008JD009944.

Johnson, M., Y. Jung, D. T. Dawson, and M. Xue, 2016: Comparison of simulated polarimetric signatures in idealized supercell storms using two-moment bulk microphysics schemes in WRF. *Mon. Wea. Rev.*, **144**, 971–996, https://doi.org/10.1175/MWR-D-15-0233.1.

Jones, T. A., and Coauthors, 2020: Assimilation of *GOES-16* radiances and retrievals into the warn-on-forecast system. *Mon. Wea. Rev.*, **148**, 1829–1859, https://doi.org/10.1175/MWR-D-19-0379.1.

Kain, J. S., and Coauthors, 2008: Some practical considerations regarding horizontal resolution in the first generation of operational convection-allowing NWP. *Wea. Forecasting*, **23**, 931–952, https://doi.org/10.1175/WAF2007106.1.

——, and Coauthors, 2013: A feasibility study for probabilistic convection initiation forecasts based on explicit numerical guidance. *Bull. Amer. Meteor. Soc.*, **94**, 1213–1225, https://doi.org/10.1175/BAMS-D-11-00264.1.

Kim, M., J. Jin, A. El Akkraoui, W. McCarty, R. Todling, W. Gu, and R. Gelaro, 2020: The framework for assimilating all-sky GPM microwave imager brightness temperature data in the NASA GEOS data assimilation system. *Mon. Wea. Rev.*, **148**, 2433–2455, https://doi.org/10.1175/MWR-D-19-0100.1.

Kirshbaum, D. J., F. Fabry, and Q. Cazenave, 2016: The Mississippi Valley convection minimum on summer afternoons: Observations and numerical simulations. *Mon. Wea. Rev.*, **144**, 263–272, https://doi.org/10.1175/MWR-D-15-0238.1.

Langhans, W., J. Schmidli, O. Fuhrer, S. Bieri, and C. Schär, 2013: Long-term simulations of thermally-driven flows and orographic convection at convection-parameterizing and cloud-resolving resolutions. *J. Appl. Meteor. Climatol.*, **52**, 1490–1510, https://doi.org/10.1175/JAMC-D-12-0167.1.

Lawson, J. R., J. S. Kain, N. Yussouf, D. C. Dowell, D. M. Wheatley, K. H. Knopfmeier, and T. A. Jones, 2018: Advancing from convection-allowing NWP to Warn-on-Forecast: Evidence of progress. *Wea. Forecasting*, **33**, 599–607, https://doi.org/10.1175/WAF-D-17-0145.1.

Lee, S., H. Han, J. Im, E. Jang, and M.-I. Lee, 2017: Detection of deterministic and probabilistic convection initiation using *Himawari-8* advanced Himawari imager data. *Atmos. Meas. Tech.*, **10**, 1859–1874, https://doi.org/10.5194/amt-10-1859-2017.

Lei, H., J. Guo, D. Chen, and J. Yang, 2020: Systematic bias in the prediction of warm-rain hydrometeors in the WDM6 microphysics scheme and modifications. *J. Geophys. Res. Atmos.*, **125**, e2019JD030756, https://doi.org/10.1029/2019JD030756.

Lim, K.-S. S., and S.-Y. Hong, 2010: Development of an effective double-moment cloud microphysics scheme with prognostic cloud condensation nuclei (CCN) for weather and climate models. *Mon. Wea. Rev.*, **138**, 1587–1612, https://doi.org/10.1175/2009MWR2968.1.

Liu, H., and M. Xue, 2008: Prediction of convective initiation and storm evolution on 12 June 2002 during IHOP_2002. Part I: Control simulation and sensitivity experiments. *Mon. Wea. Rev.*, **136**, 2261–2282, https://doi.org/10.1175/2007MWR2161.1.

Lopez, P., K. Finkele, P. Clark, and P. Mascart, 2003: Validation and intercomparison of three mesoscale models on three FASTEX cloud systems: Comparison with coarse-resolution simulations. *Quart. J. Roy. Meteor. Soc.*, **129**, 1841–1871, https://doi.org/10.1256/qj.01.113.

Mace, G. G., and F. J. Wrenn, 2013: Evaluation of the hydrometeor layers in the east and west Pacific within ISCCP cloud-top pressure–optical depth bins using merged *CloudSat* and *CALIPSO* data. *J. Climate*, **26**, 9429–9444, https://doi.org/10.1175/JCLI-D-12-00207.1.

Madaus, L. E., and G. J. Hakim, 2016: Observable surface anomalies preceding simulated isolated convective initiation. *Mon. Wea. Rev.*, **144**, 2265–2284, https://doi.org/10.1175/MWR-D-15-0332.1.

——, and ——, 2017: Constraining ensemble forecasts of discrete convective initiation with surface observations. *Mon. Wea. Rev.*, **145**, 2597–2610, https://doi.org/10.1175/MWR-D-16-0395.1.

Marshall, J. S., and S. Radhakant, 1978: Radar precipitation maps as lightning indicators. *J. Appl. Meteor.*, **17**, 206–212, https://doi.org/10.1175/1520-0450(1978)017<0206:RPMALI>2.0.CO;2.

Matthee, R., and J. R. Mecikalski, 2013: Geostationary infrared methods for detecting lightning-producing cumulonimbus

clouds. *J. Geophys. Res. Atmos.*, **118**, 6580–6592, https://doi.org/10.1002/jgrd.50485.

——, ——, L. D. Carey, and P. M. Bitzer, 2014: Quantitative differences between lightning and nonlightning convective rainfall events as observed with polarimetric radar and MSG satellite data. *Mon. Wea. Rev.*, **142**, 3651–3665, https://doi.org/10.1175/MWR-D-14-00047.1.

Mecikalski, J. R., and K. Bedka, 2006: Forecasting convective initiation by monitoring the evolution of moving cumulus in daytime GOES imagery. *Mon. Wea. Rev.*, **134**, 49–78, https://doi.org/10.1175/MWR3062.1.

——, ——, S. Paech, and L. Litten, 2008: A statistical evaluation of GOES cloud-top properties for nowcasting convective initiation. *Mon. Wea. Rev.*, **136**, 4899–4914, https://doi.org/10.1175/2008MWR2352.1.

——, W. M. Mackenzie, M. Koenig, and S. Muller, 2010: Cloud-top properties of growing cumulus prior to convective initiation as measured by Meteosat Second Generation. Part I: Infrared fields. *J. Appl. Meteor. Climatol.*, **49**, 521–534, https://doi.org/10.1175/2009JAMC2344.1.

——, P. D. Watts, and M. Koenig, 2011: Use of Meteosat Second Generation optimal cloud analysis fields for understanding physical attributes of growing cumulus clouds. *Atmos. Res.*, **102**, 175–190.

——, P. Minnis, and R. Palikonda, 2013: Use of satellite derived cloud properties to quantify growing cumulus beneath cirrus clouds. *Atmos. Res.*, **120–121**, 192–201, https://doi.org/10.1016/j.atmosres.2012.08.017.

——, J. K. Williams, C. P. Jewett, D. Ahijevych, A. LeRoy, and J. R. Walker, 2015: Probabilistic 0–1-h convective initiation nowcasts that combine geostationary satellite observations and numerical weather prediction model data. *J. Appl. Meteor. Climatol.*, **54**, 1039–1059, https://doi.org/10.1175/JAMC-D-14-0129.1.

——, D. Rosenfeld, and A. Manzato, 2016a: Evaluation of geostationary satellite observations and the development of a 1–2 h prediction model for future storm intensity. *J. Geophys. Res. Atmos*, **121**, 6374–6392, https://doi.org/10.1002/2016JD024768.

——, C. P. Jewett, J. M. Apke, and L. D. Carey, 2016b: Analysis of cumulus cloud updrafts as observed with 1–min resolution super rapid scan GOES imagery. *Mon. Wea. Rev.*, **144**, 811–830, https://doi.org/10.1175/MWR-D-14-00399.1.

Miller, P. W., and T. L. Mote, 2017: A climatology of weakly forced and pulse thunderstorms in the southeast United States. *J. Appl. Meteor. Climatol.*, **56**, 3017–3033, https://doi.org/10.1175/JAMC-D-17-0005.1.

Mittermaier, M., and R. Bullock, 2013: Using MODE to explore the spatial and temporal characteristics of cloud cover forecasts from high-resolution NWP models. *Meteor. Appl.*, **20**, 187–196, https://doi.org/10.1002/met.1393.

Morrison, H., J. A. Curry, and V. I. Khvorostyanov, 2005: A new double-moment microphysics parameterization for application in cloud and climate models. Part I: Description. *J. Atmos. Sci.*, **62**, 1665–1677, https://doi.org/10.1175/JAS3446.1.

——, G. Thompson, and V. Tatarskii, 2009: Impact of cloud microphysics on the development of trailing stratiform precipitation in a simulated squall line: Comparison of one- and two-moment schemes. *Mon. Wea. Rev.*, **137**, 991–1007, https://doi.org/10.1175/2008MWR2556.1.

——, J. A. Milbrandt, G. H. Bryan, K. Ikeda, S. A. Tessendorf, and G. Thompson, 2015: Parameterization of cloud microphysics based on the prediction of bulk ice particle properties. Part II: Case study comparisons with observations and other schemes. *J. Atmos. Sci.*, **72**, 312–339, https://doi.org/10.1175/JAS-D-14-0066.1.

Mueller, C. K., T. Saxen, R. Roberts, J. Wilson, T. Betancourt, S. Dettling, N. Oien, and J. Yee, 2003: NCAR Auto-Nowcast system. *Wea. Forecasting*, **18**, 545–561, https://doi.org/10.1175/1520-0434(2003)018<0545:NAS>2.0.CO;2.

Niu, G.-Y., and Coauthors, 2011: The community Noah land surface model with multiparameterization options (Noah-MP): 1. Model description and evaluation with local-scale measurements. *J. Geophys. Res.*, **116**, D12109, https://doi.org/10.1029/2010JD015139.

Otkin, J. A., and T. J. Greenwald, 2008: Comparison of WRF model-simulated and MODIS-derived cloud data. *Mon. Wea. Rev.*, **136**, 1957–1970, https://doi.org/10.1175/2007MWR2293.1.

——, D. J. Posselt, E. R. Olson, H.-L. Huang, J. E. Davies, J. Li, and C. S. Velden, 2007: Mesoscale numerical weather prediction models used in support of infrared hyperspectral measurement simulation and product algorithm development. *J. Atmos. Oceanic Technol.*, **24**, 585–601, https://doi.org/10.1175/JTECH1994.1.

——, T. J. Greenwald, J. Sieglaff, and H.-L. Huang, 2009: Validation of a large-scale simulated brightness temperature dataset using SEVIRI satellite observations. *J. Appl. Meteor. Climatol.*, **48**, 1613–1626, https://doi.org/10.1175/2009JAMC2142.1.

Patou, M., J. Vidot, J. Riédi, G. Penide, and T. J. Garrett, 2018: Prediction of the onset of heavy rain using SEVIRI cloud observations. *J. Appl. Meteor. Climatol.*, **57**, 2343–2361, https://doi.org/10.1175/JAMC-D-17-0352.1.

Rickenbach, T. M., R. Nieto-Ferreira, C. Zarzar, and B. Nelson, 2015: A seasonal and diurnal climatology of precipitation organization in the southeastern United States. *Quart. J. Roy. Meteor. Soc.*, **141**, 1938–1956, https://doi.org/10.1002/qj.2500.

——, ——, and H. Wells, 2020: Springtime onset of isolated convection precipitation across the southeastern United States: Framework and regional evolution. *Mon. Wea. Rev.*, **148**, 891–906, https://doi.org/10.1175/MWR-D-19-0279.1.

Roberts, R. D., and S. Rutledge, 2003: Nowcasting storm initiation and growth using *GOES-8* and WSR-88D data. *Wea. Forecasting*, **18**, 562–584, https://doi.org/10.1175/1520-0434(2003)018<0562:NSIAGU>2.0.CO;2.

Schmit, T. J., P. Griffith, M. M. Gunshor, J. M. Daniels, S. J. Goodman, and W. J. Lebair, 2017: A closer look at the ABI on the GOES-R series. *Bull. Amer. Meteor. Soc.*, **98**, 681–698, https://doi.org/10.1175/BAMS-D-15-00230.1.

Schreiber, W. E., 1986: Case study of thunderstorms initiated by radar-observed convergence lines. *Mon. Wea. Rev.*, **114**, 2256–2266, https://doi.org/10.1175/1520-0493(1986)114<2256:CSOTIB>2.0.CO;2.

Schwartz, C. S., and Coauthors, 2009: Next-day convection-allowing WRF model guidance: A second look at 2-km versus 4-km grid spacing. *Mon. Wea. Rev.*, **137**, 3351–3372, https://doi.org/10.1175/2009MWR2924.1.

Senf, F., and H. Deneke, 2017: Satellite-based characterization of convective growth and glaciation and its relationship to precipitation formation over central Europe. *J. Appl. Meteor. Climatol.*, **56**, 1827–1845, https://doi.org/10.1175/JAMC-D-16-0293.1.

Shrestha, D. L., D. E. Robertson, Q. J. Wang, T. C. Pagano, and H. A. P. Hapuarachchi, 2013: Evaluation of numerical weather prediction model precipitation forecasts for short-term streamflow forecasting purpose. *Hydrol. Earth Syst. Sci.*, **17**, 1913–1931.

Sieglaff, J. M., L. M. Cronce, W. F. Feltz, K. M. Bedka, M. J. Pavolonis, and A. K. Heidinger, 2011: Nowcasting convective

storm initiation using satellite-based box-averaged cloud-top cooling and cloud-type trends. *J. Appl. Meteor. Climatol.*, **50**, 110–126, https://doi.org/10.1175/2010JAMC2496.1.

Sobash, R. A., and D. J. Stensrud, 2015: Assimilating surface mesonet observations with the EnKF to improve ensemble forecasts of convection initiation on 29 May 2012. *Mon. Wea. Rev.*, **143**, 3700–3725, https://doi.org/10.1175/MWR-D-14-00126.1.

Thompson, G., P. R. Field, R. M. Rasmussen, and W. D. Hall, 2008: Explicit forecasts of winter precipitation using an improved bulk microphysics scheme. Part II: Implementation of a new snow parameterization. *Mon. Wea. Rev.*, **136**, 5095–5115, https://doi.org/10.1175/2008MWR2387.1.

——, M. Tewari, K. Ikeda, S. Tessendorf, C. Weeks, J. Otkin, and F. Kong, 2016: Explicitly-coupled cloud physics and radiation parameterizations and subsequent evaluation in WRF high-resolution convective forecasts. *Atmos. Res.*, **168**, 92–104, https://doi.org/10.1016/j.atmosres.2015.09.005.

Tiedtke, M., 1989: A comprehensive mass flux scheme for cumulus parameterization in large-scale models. *Mon. Wea. Rev.*, **117**, 1779–1800, https://doi.org/10.1175/1520-0493(1989)117<1779:ACMFSF>2.0.CO;2.

Tselioudis, G., and C. Jakob, 2002: Evaluation of midlatitude cloud properties in a weather and a climate model: Dependence on dynamic regime and spatial resolution. *J. Geophys. Res.*, **107**, 4781, https://doi.org/10.1029/2002JD002259.

Vila, D. A., L. A. T. Machado, H. Laurent, and I. Velasco, 2008: Forecast and Tracking the Evolution of Cloud Clusters (ForTraCC) using satellite infrared imagery: Methodology and validation. *Wea. Forecasting*, **23**, 233–245, https://doi.org/10.1175/2007WAF2006121.1.

Virtanen, P., and Coauthors, 2020: SciPy 1.0: Fundamental algorithms for scientific computing in Python. *Nat. Methods*, **17**, 261–272, https://doi.org/10.1038/s41592-019-0686-2.

Walker, J. R., W. M. MacKenzie, J. R. Mecikalski, and C. P. Jewett, 2012: An enhanced geostationary satellite–based convective initiation algorithm for 0–2-h nowcasting with object tracking. *J. Appl. Meteor. Climatol.*, **51**, 1931–1949, https://doi.org/10.1175/JAMC-D-11-0246.1.

Wall, C. J., D. L. Hartmann, M. M. Thieman, W. L. Smith, and P. Minnis, 2018: The life cycle of anvil clouds and the top-of-atmosphere radiation balance over the tropical west Pacific. *J. Climate*, **31**, 10 059–10 080, https://doi.org/10.1175/JCLI-D-18-0154.1.

Weckwerth, T. M., and D. B. Parsons, 2006: A review of convective initiation and motivation for IHOP_2002. *Mon. Wea. Rev.*, **134**, 5–22, https://doi.org/10.1175/MWR3067.1.

Weisman, M. L., C. Davis, W. Wang, K. W. Manning, and J. B. Klemp, 2008: Experiences with 0–36-h explicit convective forecasts with the WRF-ARW model. *Wea. Forecasting*, **23**, 407–437, https://doi.org/10.1175/2007WAF2007005.1.

Wilson, J. W., and W. E. Schriber, 1986: Initiation of convective storms by radar-observed boundary layer convergent lines. *Mon. Wea. Rev.*, **114**, 2516–2536, https://doi.org/10.1175/1520-0493(1986)114<2516:IOCSAR>2.0.CO;2.

——, and C. K. Mueller, 1993: Nowcasts of thunderstorm initiation and evolution. *Wea. Forecasting*, **8**, 113–131, https://doi.org/10.1175/1520-0434(1993)008<0113:NOTIAE>2.0.CO;2.

——, G. B. Foote, N. A. Crook, J. C. Fankhauser, C. G. Wade, J. D. Tuttle, C. K. Mueller, and S. K. Krueger, 1992: The role of boundary layer convergence zones and horizontal rolls in the initiation of thunderstorms: A case study. *Mon. Wea. Rev.*, **120**, 1785–1815, https://doi.org/10.1175/1520-0493(1992)120<1785:TROBLC>2.0.CO;2.

Yussouf, N., D. C. Dowell, L. J. Wicker, K. H. Knopfmeier, and D. M. Wheatley, 2015: Storm-scale data assimilation and ensemble forecasts for the 27 April 2011 severe weather outbreak in Alabama. *Mon. Wea. Rev.*, **143**, 3044–3066, https://doi.org/10.1175/MWR-D-14-00268.1.

Zhang, C., Y. Wang, and K. Hamilton, 2011: Improved representation of boundary layer clouds over the southeast Pacific in ARW–WRF using a modified Tiedtke cumulus parameterization scheme. *Mon. Wea. Rev.*, **139**, 3489–3513, https://doi.org/10.1175/MWR-D-10-05091.1.

Zhang, Y., D. J. Stensrud, and F. Zhang, 2019: Simultaneous assimilation of radar and all-sky satellite infrared radiance observations for convection-allowing ensemble analysis and prediction of severe thunderstorms. *Mon. Wea. Rev.*, **147**, 4389–4409, https://doi.org/10.1175/MWR-D-19-0163.1.

Zipser, E. J., 2003: Some views on ''hot towers'' after 50 years of tropical field programs and two years of TRMM data. *Cloud Systems, Hurricanes, and the Tropical Rainfall Measuring Mission (TRMM)*, *Meteor. Monogr.*, No. 51, Amer. Meteor. Soc., 49–58.